

## OBSERVATIONAL EVIDENCE OF SUPERSHELL BLOWOUT IN GS 018–04+44: THE SCUTUM SUPERSHELL<sup>1</sup>

MATTHEW B. CALLAWAY,<sup>2</sup> BLAIR D. SAVAGE,<sup>3</sup> ROBERT A. BENJAMIN,<sup>2</sup>  
L. MATTHEW HAFFNER,<sup>3</sup> AND STEVE L. TUFTE<sup>3</sup>

Received 1999 June 2; accepted 1999 November 10

### ABSTRACT

Emission in the H I 21 cm line has been mapped for a region of the Galaxy that includes two known supershells, GS 018–04+44 and GS 034–06+65. We focus on the GS 018–04+44, hereafter referred to as the Scutum Supershell, which is an elongated shell about 5° in diameter extending to –7° below the Galactic plane. The Scutum shell lies at a kinematic distance of ~3300 pc, implying a shell diameter of ~290 pc with a vertical extension of ~400 pc away from the Galactic plane. The Scutum shell contains  $6.2 \times 10^5 M_{\odot}$  swept into the walls. We observe that the top of the shell is missing, and a substantial column of H I rises from the shell walls to  $b = -11^{\circ}$ , culminating in a large cloud of neutral hydrogen,  $3.74 \times 10^4 M_{\odot}$ , located ~630 pc from the plane. *ROSAT* data show X-ray emission that closely anticorrelates with the 21 cm emission. This emission probably originates from hot gas within the Scutum Supershell. After approximately correcting for the foreground absorption, we find that the 1.5 keV X-rays peak at the base of the shell, the 0.75 keV emission peaks in the interior and at the top of the shell, and the 0.25 keV emission extends to high latitudes above the shell. The X-ray luminosity is roughly  $\sim 5 \times 10^{36}$  ergs s<sup>-1</sup>. The Wisconsin H-Alpha Mapper (WHAM) survey shows the presence of H $\alpha$  emission that exhibits a morphology similar to that of the H I. Spectra indicate the presence of ionized hydrogen at velocities similar to the H I, placing ionized material at the same kinematic distance as the neutral material. *IRAS* images in the 60 and 100  $\mu$ m wavebands reveal the presence of dust correlated with the neutral hydrogen. Infrared surface brightness indicates an excess in the 100  $\mu$ m emission, which could indicate a molecular hydrogen component with a column density of  $2.4 \times 10^{21}$  cm<sup>-2</sup> in the densest regions of the high-latitude cloud of neutral hydrogen. *IUE* ultraviolet high dispersion spectra of HD 177989 ( $l = 17^{\circ}89$ ,  $b = -11^{\circ}88$ ) and HD 175754 ( $l = 16^{\circ}40$ ,  $b = -9^{\circ}92$ ) reveal the presence of very strong absorption by highly ionized gas at a velocity that associates the absorption with the ejecta of the Scutum Supershell. In the case of HD 177989, the high ion column density ratios suggest an origin in a turbulent mixing layer where hot and cool gases mix in the presence of shear flows. The H $\alpha$  and X-ray emission suggest that a multitude of energetic phenomena exist in this region, providing the necessary ionizing radiation. Indeed, there are multiple supernova remnants, H II regions, and hot stars, which could all contribute sizeable amounts of energy and ionizing radiation. The combination of these data sets indicates observational evidence of a “blowout” phenomena whereby hot material produced within the Scutum Supershell has blown through the top of the shell and been pushed to high latitude.

*Subject headings:* Galaxy: structure — ISM: bubbles — ISM: individual (Scutum Supershell) —  
ISM: structure — radio lines: ISM — supernova remnants

### 1. INTRODUCTION

The structure of the 21 cm H I sky displays a variety of features including shells, holes, and arclike structures. Holes and shells of various sizes have been found in the Milky Way and other nearby galaxies (Heiles 1979, 1984; Brinks & Bajaja 1986; Deul & den Hartog 1990; Kamphuis, Sancisi, & van der Hulst 1991; Chu et al. 1993, 1995). Dominant theories explaining Galactic shells attribute them to the collective effects of energetic phenomena such as supernovae and stellar winds from OB associations (Tenorio-Tagle & Bodenheimer 1988). Winds and explosions in the Galactic disk create a bubble of material that expands within a stratified medium. Upon reaching a few times the scale height of the Galactic disk, the hot material within the bubble can escape to the halo in the “blowout” phenom-

non, where material is ejected through the thick disk of the Galaxy into the Galactic halo (Heiles 1990). Such phenomena are thought to evacuate regions of the Galaxy and sweep material into their observed morphological shapes (Heiles 1979, 1984; Maciejewski et al. 1996). Understanding the processes that create shells is an important step in understanding the structure of the ISM and the distribution of matter in the Galactic disk and halo.

This paper attempts to correlate data from various surveys and develop a complete picture of a Galactic supershell. The Scutum Shell, located at Galactic longitude 17:5 and latitude –4:0, has been noted in previous surveys (Heiles 1979) as GS 016–06+43. Recent H I data indicate that a more accurate identification is GS 018–4+44. It is clear from the 21 cm radio data presented in this paper that this region displays complex structure, but we turn to data sets in other wavelengths to clarify the physics of the region. We shall present data in 21 cm radio emission, *ROSAT*/*PSPC* X-ray data, H $\alpha$  data from the Wisconsin H $\alpha$  Mapper (WHAM), *IRAS* 60 and 100  $\mu$ m data, and UV spectra of several stars in the Scutum shell region. These data clarify the morphology of the object itself and provide several tools

<sup>1</sup> Based on observations from the Green Bank 43m radio telescope, the *ROSAT* All-Sky Survey, the WHAM All-Sky Survey, *IRAS*, and *IUE*.

<sup>2</sup> Department of Physics, University of Wisconsin, 1150 University Avenue, Madison, WI 53706.

<sup>3</sup> Department of Astronomy, University of Wisconsin, 475 North Charter Street, Madison, WI 53706.

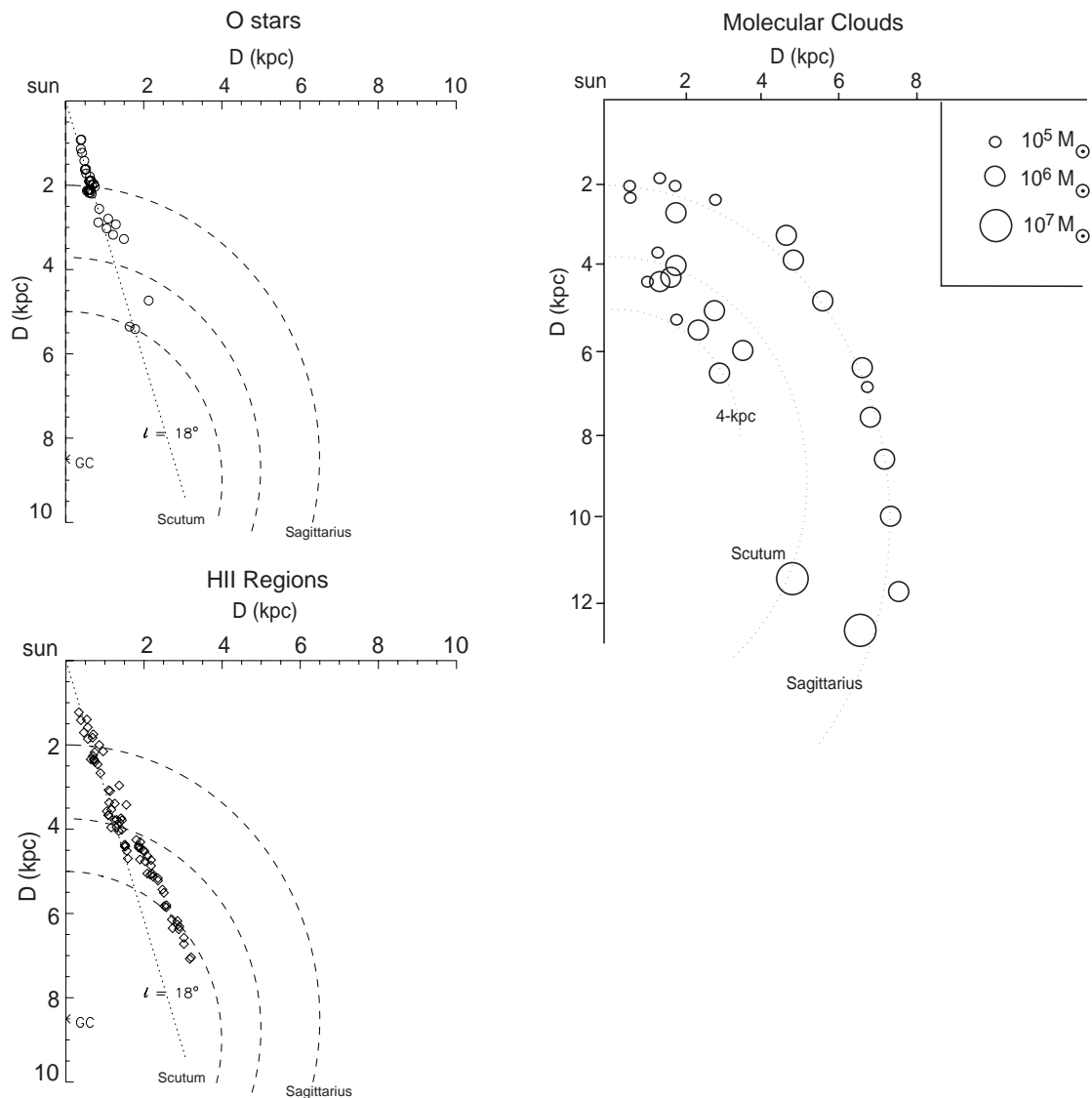


FIG. 1.—Superposition of objects along the sight line toward  $l = 18^\circ$ , the Scutum region. *Top left*: O stars from Garmany's catalog. *Bottom left*: H II regions from the Lockman survey. *Right*: Recreation Fig. 9 of Dame et al. (1986) displaying molecular clouds. Note that they use a different value of distance to Galactic center. Note also that we have assumed that the objects lie on the near side of the tangent point. We attempt to focus on the Scutum shell region, at a distance of 3.3 kpc, and identify which objects may be associated with this region. The dashed curves on the plots very roughly delineate the positions of the Sagittarius and Scutum spiral arms as traced by the molecular clouds. Delineating the actual positions of spiral arms is a very subjective process.

to analyze the kinematics of the shell. We also take note of related objects such as H II regions, O and B stars, and supernova remnants that could be associated with the shell and that may have roles in the production and evolution of the shell.

Interstellar absorption features also provide information on the high-latitude ejecta of the shell. *IUE* spectra of HD 177989 ( $l = 17^\circ 9$ ,  $b = -11^\circ 9$ ) and HD 175754 ( $l = 16^\circ 4$ ,  $b = -9^\circ 9$ ) sample sight lines penetrating a high-latitude cloud of gas thought to have originated in the Scutum shell. We analyze these spectra to provide information about the nature of the ionized species associated with the shell ejecta. The spectra support our claim that the material lies at the same kinematic distance as the Scutum shell.

The sight line toward the Scutum shell is complicated by a superposition of objects associated with Galactic spiral arms. An introduction to the line of sight follows in § 2. This discussion is followed by the presentation of the obser-

vational data in § 3, including observations of H I 21 cm and *IRAS* 60 and 100  $\mu\text{m}$  emission, X-rays at 0.25 keV, 0.75 keV, and 1.5 keV, H $\alpha$  emission, and the *IUE* spectra of the stars HD 177989, HD 175754, and HD 175876. Section 4 presents summary of objects related to the Scutum shell. In § 5 we derive the principal physical characteristics of the Scutum Supershell from the data. A comparison of the Scutum shell with other supershells is presented in § 6, and finally we present the interpretation and implications of this analysis in § 7.

## 2. GALACTIC ENVIRONMENT

The Scutum Supershell lies in the direction  $l = 17^\circ 5$ ,  $b = -4^\circ 0$ . This line of sight passes through the inner part of the local spiral arm and two more distant arms: the Sagittarius arm at a velocity of  $+20 \text{ km s}^{-1}$ , corresponding to a kinematic distance of  $\sim 2 \text{ kpc}$ , and the Norma-Scutum arm at  $+40 \text{ km s}^{-1}$ , at a distance of 3–4 kpc (according to the

TABLE 1  
H II REGIONS (REPRODUCED FROM LOCKMAN 1989)

$l$ (deg)	$b$ (deg)	$V_{\text{LSR}}$ (km s $^{-1}$ )	$T_L$ (mK)	FWHM (km s $^{-1}$ )	Notes
15.032.....	-0.687	16.8	1722 $\pm$ 26.7	37.3 $\pm$ 0.7	M17
15.143.....	-0.940	11.9	38 $\pm$ 5.3	40.4 $\pm$ 6.5	...
15.181.....	-0.625	13.9	229 $\pm$ 7.7	29.4 $\pm$ 1.1	...
15.198.....	-0.768	23.8	108 $\pm$ 7.6	21.3 $\pm$ 1.7	S45
16.313.....	-0.162	49.5	39 $\pm$ 2.4	21.9 $\pm$ 1.5	...
16.368.....	-0.515	42.7	71 $\pm$ 6.5	15.2 $\pm$ 1.7	...
16.431.....	-0.199	44.5	29 $\pm$ 2.2	24.0 $\pm$ 2.1	...
16.614.....	-0.324	44.9	39 $\pm$ 2.7	16.2 $\pm$ 1.3	S48
16.808.....	-0.072	20.4	32 $\pm$ 3.5	25.1 $\pm$ 3.5	S50
16.936.....	0.758	26.3	119 $\pm$ 4.6	26.3 $\pm$ 1.2	...
16.984.....	0.934	25.4	119 $\pm$ 6.6	26.2 $\pm$ 1.7	...
16.995.....	0.868	26.7	113 $\pm$ 8.8	26.6 $\pm$ 2.4	...
17.144.....	0.765	27.4	57 $\pm$ 6.3	20.4 $\pm$ 2.6	...
18.143.....	-0.289	53.9	148 $\pm$ 5.1	23.7 $\pm$ 0.9	...
18.185.....	-0.397	43.2	60 $\pm$ 4.5	20.1 $\pm$ 1.8	...
18.197.....	-0.181	46.1	23 $\pm$ 2.2	26.4 $\pm$ 3.1	...
18.252.....	1.892	29.8	51 $\pm$ 4.4	25.1 $\pm$ 2.5	S54
18.258.....	-0.297	50.9	65 $\pm$ 3.6	30.1 $\pm$ 1.9	S53
18.305.....	-0.391	32.7	52 $\pm$ 5.5	29.3 $\pm$ 3.6	...
18.456.....	-0.007	56.5	26 $\pm$ 2.2	32.1 $\pm$ 3.2	...
18.686.....	1.965	26.6	112 $\pm$ 6.5	23.7 $\pm$ 1.6	...
18.881.....	-0.493	65.5	92 $\pm$ 5.3	27.1 $\pm$ 1.8	S54
18.954.....	-0.019	52.3	26 $\pm$ 2.5	36.1 $\pm$ 3.9	...
19.044.....	-0.431	65.8	53 $\pm$ 6.0	23.5 $\pm$ 3.1	...
19.050.....	-0.593	68.2	36 $\pm$ 3.7	18.6 $\pm$ 2.2	...
19.066.....	-0.281	64.9	121 $\pm$ 5.3	22.5 $\pm$ 1.1	...
19.485.....	0.138	19.8	56 $\pm$ 3.4	17.5 $\pm$ 1.2	...
19.608.....	-0.235	41.0	131 $\pm$ 7.4	27.7 $\pm$ 1.8	...
19.614.....	-0.132	58.6	54 $\pm$ 3.7	22.8 $\pm$ 1.8	...
19.671.....	-0.137	55.0	48 $\pm$ 5.8	20.0 $\pm$ 2.8	...
20.074.....	-0.141	42.2	31 $\pm$ 2.8	31.7 $\pm$ 3.3	...
20.264.....	-0.894	47.7	33 $\pm$ 3.4	19.7 $\pm$ 2.6	S55
20.479.....	0.165	24.1	24 $\pm$ 2.3	20.5 $\pm$ 2.2	...
20.681.....	-0.136	55.2	63 $\pm$ 4.3	23.4 $\pm$ 1.9	...
20.733.....	-0.087	56.3	93 $\pm$ 4.5	26.2 $\pm$ 1.1	...
20.988.....	0.092	18.6	47 $\pm$ 5.6	21.4 $\pm$ 2.9	...
21.871.....	0.008	24.4	24 $\pm$ 3.4	24.3 $\pm$ 4.0	...
23.115.....	0.556	29.5	17 $\pm$ 1.2	28.0 $\pm$ 2.2	S58
23.909.....	0.066	32.8	16 $\pm$ 2.8	15.7 $\pm$ 3.3	...
24.303.....	-0.151	55.5	24 $\pm$ 2.6	21.4 $\pm$ 3.3	...
24.742.....	-0.207	47.5	12 $\pm$ 4.0	19.5 $\pm$ 7.6	...

rotation curve of Clemens 1985). These arms can be seen in several spiral arm tracers including H II regions (Lockman 1989; Blitz, Fich, & Stark 1982), molecular clouds (Dame et al. 1986), and O stars (Garmany, Conti, & Chiosi 1982). Unless otherwise noted, all velocities quoted in this paper are referenced to the local standard of rest (LSR).

The two left panels of Figure 1 show the distribution of O stars and H II regions along the sight line toward the Scutum Supershell, in the Galactic longitude range  $l = 14^\circ$ – $24^\circ$ . The lower left panel displays H II regions from Lockman (1989), listed on Table 1. Kinematic distances to these H II regions are based on the Galactic rotation curve of Clemens (1985), assuming that objects lie on the near side of the tangent point. The upper left panel displays O stars from Garmany et al. (1982), which are listed on Table 2. Distances to O stars are based on cluster or association membership, or from the observed apparent magnitude, assuming the Conti (1975) calibration of spectral type and  $M_V$  together with the extinction correction  $A_V = 3.1E(B-V)$ . The right panel in Figure 1 displays molecular

clouds from Dame et al. (1986), with distances according to the Clemens rotation curve. The Dame et al. study of molecular clouds also illustrates the spiral arm structure (see their Figs. 9, 10a, and 10b).

The molecular clouds and H II regions shown in Figure 1 are grouped at  $d \sim 2$  kpc, corresponding to the  $v \sim +20$  km s $^{-1}$  Sagittarius arm, and at  $d \sim 3$ – $4$  kpc, corresponding to the  $v \sim +40$  to  $+50$  km s $^{-1}$  Norma-Scutum arm. The O star distribution reveals a clumping associated with the Sagittarius spiral arm and clumping at  $\sim 3$  kpc that may represent the near side of the Norma-Scutum spiral arm. In our multiwavelength analysis, we will separate emission and absorption due to material associated with these spiral structures.

### 3. OBSERVATIONAL DATA

In the following sections, we present data sets in all wavebands used to study the Scutum Supershell. A synthesis and analysis of the information to infer the physical characteristics of the supershell is presented in § 5. The data sets include the following: 21 cm H I observations from the NRAO radio telescope; infrared observations in the 60 and 100  $\mu$ m wavebands of the *IRAS* instrument; X-ray observations at the 0.25, 0.75 and 1.50 keV energy from the all-sky X-ray maps from the *Röntgen Satellit (ROSAT)* instrument; H $\alpha$  observations from the Wisconsin H $\alpha$  Mapper (WHAM); and UV absorption spectroscopy from the *International Ultraviolet Explorer* satellite (*IUE*).

#### 3.1. H I Data

The 21 cm radio data were obtained with the 43 m radio telescope at Green Bank, W. Virginia, during the month of August in 1990, 1991, and 1992 (hereafter referred to as the NRAO H I survey). These are the same data used by Maciejewski et al. (1996) in their study of the Aquila Supershell. The telescope has an angular resolution of 21' (FWHM) at the 21 cm wavelength. Spectra cover the range of velocities  $-200$  km s $^{-1}$  to  $+200$  km s $^{-1}$  with respect to the LSR at a velocity resolution of 1 km s $^{-1}$ . The 21 cm line emission for this survey ranges over Galactic longitudes  $11^\circ \leq l \leq 40^\circ$  and Galactic latitudes  $-15^\circ \leq b \leq -0.5^\circ$ . Spectra were always taken every 10' in latitude and, for most of the mapped region, every 10' in longitude. Each position was observed for 20 s. The result of the observations is a cube containing the values of 21 cm column density per unit velocity as a function of Galactic longitude, Galactic latitude, and radial velocity. Some areas of the cube have been blanked because of incomplete coverage or bad data. Further details may be found in Maciejewski et al. (1996). In the following descriptions, we use the term “above” to refer to the absolute distance  $|z|$  from the Galactic plane (e.g., an object at  $b = -5^\circ$  is “above” one at  $b = -4^\circ$ ).

The top image in Figure 2 displays a gray-scale representation of the observed region in the 21 cm emission at  $+44 \pm 1$  km s $^{-1}$ . The observed column density in the 2 km s $^{-1}$  wide velocity interval has been multiplied by  $\sin |b|$  to suppress the brighter emission near the Galactic plane. The prominent shell at  $l = 35^\circ$  is the Aquila shell, studied by Maciejewski et al. At  $l = 17.5^\circ$ , between  $b = -6^\circ$  and  $-11^\circ$ , we see the column of H I that rises from one wall of the Scutum shell. The subimage in Figure 2 focuses on the Scutum shell. The diagram in Figure 2 indicates dominant features of the H I corresponding column density map. Figure 3 is a series of images of the column density of H I

TABLE 2  
DATA FOR O STARS IN THE SCUTUM SHELL REGION<sup>a</sup>

HD	<i>l</i> (deg)	<i>b</i> (deg)	Spectral Type	<i>B</i> (mag)	<i>B</i> − <i>V</i> (mag)	<i>M</i> ( <i>V</i> ) (mag)	<i>M</i> <sub>bol</sub> (mag)	<i>d</i> (kpc)
HD 167633 .....	14.30	−00.60	O6. V	8.14	0.27	−5.30	−09.14	2.2
BD −14 4922 .....	15.20	+01.70	O9.5 II	9.73	0.85	−5.40	−08.41	2.2
HD 175876 .....	15.30	−10.58	O6.5 III	6.95	−0.10	−5.50	−09.18	2.3
BD −16 4826 .....	15.30	−00.70	O5.	9.89	0.76	−5.10	−09.33	2.2
BD −15 4930 .....	16.10	−00.10	O6.	9.42	0.74	−5.50	−09.34	2.2
HD 168444 .....	16.22	−00.00	O8. V	8.86	0.00	−4.50	−07.91	3.0
HD 175754 .....	16.38	−09.90	O8. III	7.04	−0.07	−5.50	−08.91	2.3
BD −13 4921 .....	16.90	+00.87	O9. V	9.85	0.49	−4.30	−07.55	2.2
BD −13 4927 .....	16.90	+00.80	O5.	10.08	0.84	−5.10	−09.33	2.2
HD 168917 .....	16.90	−00.30	O9. V	8.44	0.43	−4.90	−08.15	1.7
HD 168076 .....	16.90	+00.80	O4. V	8.24	0.44	−5.70	−10.17	2.2
HD 168075 .....	16.90	+00.80	O6.5 III	8.77	0.44	−5.20	−08.88	2.2
BD −13 4930 .....	16.90	+00.80	O9.5 V	9.44	0.30	−4.10	−07.23	2.2
NGC 6611 166 .....	16.92	+00.87	O9. V	10.35	0.60	−4.30	−07.55	2.3
BD −13 4923 .....	16.97	+00.90	O6.	10.08	0.85	−5.30	−09.14	2.2
BD −13 4929 .....	16.98	+00.80	O9.5 V	9.86	0.60	−4.20	−07.33	1.8
HD 168137 .....	17.00	+00.80	O8. V	8.95	0.39	−4.90	−08.31	2.2
HD 168504 .....	17.02	+00.35	O8. III	9.20	0.00	−5.50	−08.91	5.6
HD 169755 .....	17.20	−01.30	O8. V	9.26	0.53	−4.40	−07.81	1.7
HD 167330 .....	17.60	+02.20	O9. I	8.23	0.66	−6.20	−09.33	2.0
BD −13 4941 .....	17.80	+00.90	O9.5 IV	9.75	1.08	−5.89	−09.02	2.0
HD 169727 .....	18.00	−00.80	O6.	9.28	0.80	−5.20	−09.04	1.7
BD −12 4964 .....	18.10	+01.80	O8.	9.82	0.91	−5.40	−08.81	2.0
BD −12 4979 .....	18.23	+01.72	O7. F	10.44	0.68	−6.40	−09.81	5.7
HD 167971 .....	18.30	+01.70	O8. I	7.50	0.77	−7.20	−10.45	2.0
BD −12 4975 .....	18.30	+01.70	O7. F	10.44	0.68	−4.10	−07.51	2.0
BD −12 4984 .....	18.50	+01.80	O8. V	9.93	0.83	−5.00	−08.41	2.0
BD −12 4994 .....	18.50	+01.60	O9. V	9.81	0.70	−4.70	−07.95	2.0
HD 168112 .....	18.50	+01.60	O5. III	8.52	0.69	−6.00	−10.23	2.0
HD 168461 .....	18.57	+01.25	O8. IV	9.54	0.68	−5.10	−08.51	2.1
BD −13 5015 .....	18.60	−01.80	O7.	10.02	0.53	−4.80	−08.36	2.7
BD −12 5009 .....	18.60	+01.30	O8.	9.54	0.68	−4.90	−08.31	2.0
HD 171589 .....	18.65	−03.10	O7.5 V	8.28	0.32	−4.60	−08.08	1.5
HD 166734 .....	18.92	+03.62	O7.5 I	8.42	1.09	−6.40	−09.73	1.3
HD 170452 .....	18.98	−01.22	O9. V	8.75	0.53	−4.30	−07.55	1.2
BD −11 4586 .....	19.10	+02.10	O8. I	9.40	1.00	−6.00	−09.25	2.0
BD −11 4620 .....	19.15	+00.68	O5.	10.17	0.80	−5.80	−10.03	3.2
BD −12 5039 .....	19.17	+00.33	O6.	10.77	1.18	−5.30	−09.14	1.9
BD −12 5104 .....	20.00	−01.70	O7.	9.55	0.58	−4.80	−08.36	2.1
HD 171198 .....	20.03	−01.73	O7.	9.54	0.57	−4.80	−08.36	2.1
BD −10 4682 .....	20.30	+10.00	O7.	9.63	0.56	−4.80	−08.36	2.2
BD −11 4674 .....	20.97	−01.20	O9.5 I	10.18	1.11	−6.70	−09.71	3.4
HD 169582 .....	21.32	+01.22	O5. I	8.70	0.56	−6.40	−10.44	3.0
BD −08 4617 .....	22.80	+01.00	O8.5 V	9.36	0.91	−4.30	−07.63	1.0
HD 173010 .....	23.73	−02.50	O9.5 I	9.18	0.83	−6.70	−09.71	3.2
BD −08 4634 .....	23.80	+00.10	O9. V	9.44	0.91	−4.20	−07.45	1.0
HD 173783 .....	24.18	−03.35	O9. I	9.31	0.51	−6.70	−09.83	5.2
HD 172175 .....	24.50	−00.80	O6. F	9.44	0.63	−6.30	−09.98	3.6

<sup>a</sup> From Garmany et al. 1982.

emission in the 2 km s<sup>−1</sup> wide velocity planes, also multiplied by sin |*b*|. We focus our attention on the shell structure seen toward *l* = 17°5, *b* = −4°0, and *v* = +44 km s<sup>−1</sup>. Koo, Heiles, & Reach (1992) identify this region in H I 21 cm and *IRAS* 100 and 60 μm maps, describing the feature as a “galactic worm.” Their catalog lists the structure and its surroundings as GW 14.9–1.6, GW 16.9–3.8, and GW 19.5–6.4. Koo et al. note, and we confirm, that GW 14.9–1.6 and GW 16.9–3.8 are actually the walls of a supershell, specifically the structure we now refer to as the Scutum Supershell.

The series of images in Figure 3 display the morphologi-

cal evolution of the shell through velocity space. The two notable features are the shell itself, lying between *b* = −1° and −6°, and the high-latitude cloud, lying between *b* = −9° and −12°. The shell structure lies between velocities +38 km s<sup>−1</sup> and +68 km s<sup>−1</sup>. It is most visible at +44 km s<sup>−1</sup>, where it subtends roughly 5° in latitude and longitude. The top of the shell, at *b* = −6° is not seen. Instead, we see a void, with a vertical column of H I rising around *l* = 18°, culminating in the large cloud centered at *l* = 18° and *b* = −11°.

We see the shell structure most clearly in the H I 21 cm images at velocities in the +40 to +50 km s<sup>−1</sup> range, where

## NRAO HI survey at 44 km/s

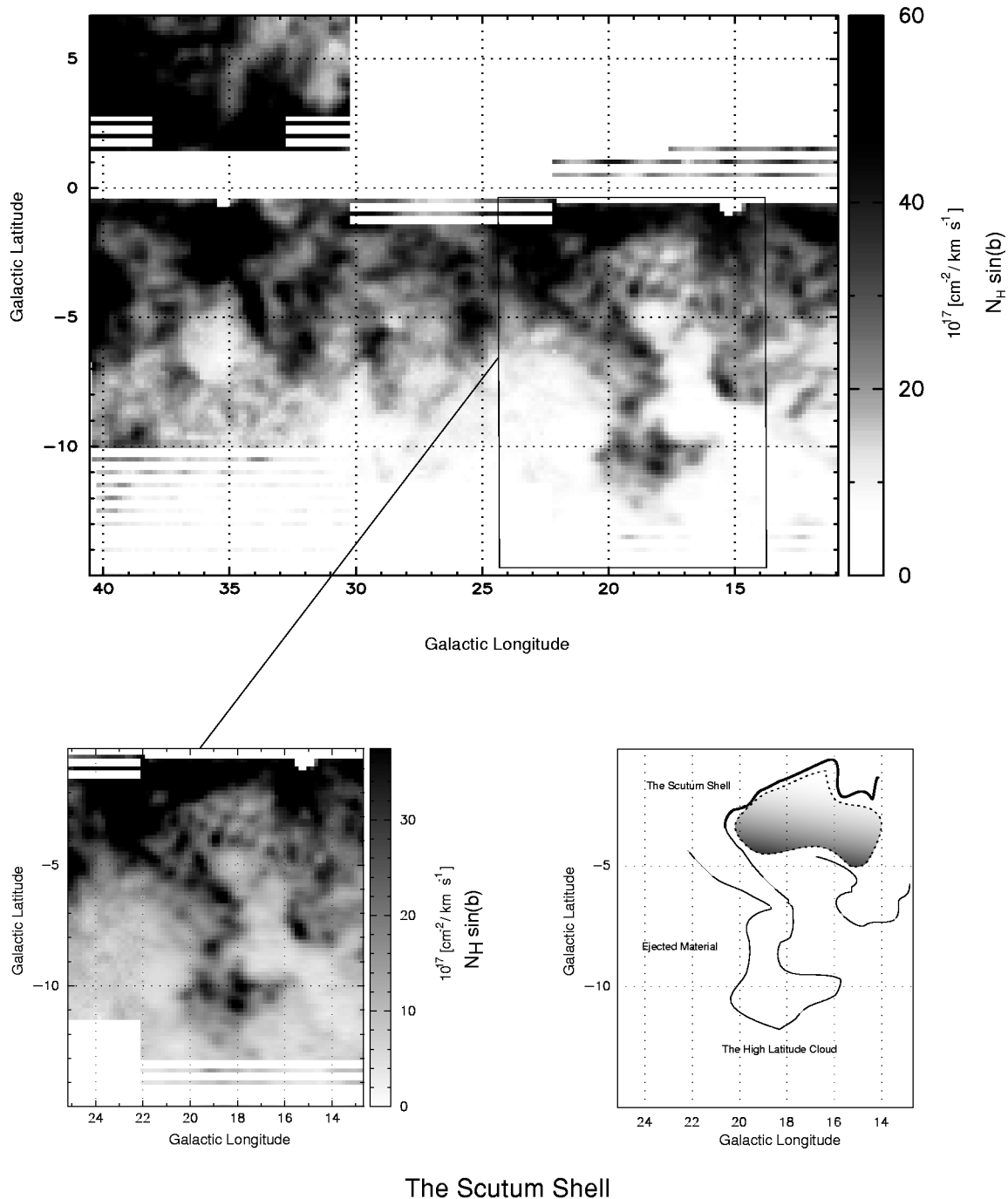


FIG. 2.—*Top*: Entire observed region in the NRAO H I survey  $+44 \pm 1 \text{ km s}^{-1}$  LSR velocity plane. The observed H I column density in the  $2 \text{ km s}^{-1}$  wide velocity interval has been multiplied by  $\sin |b|$  to enhance the contrast of the structures away from the Galactic plane. The two prominent features are the Scutum shell and its ejecta, the high-latitude cloud. The Scutum Supershell region is at the centroid velocity  $+44 \text{ km s}^{-1}$ . The diagram on the lower right displays the dominant features of the H I column density map on the lower left. The roughly spherical shell is centered at  $l = 17^{\circ}5$ ,  $b = -4^{\circ}0$ . The open top is clearly apparent, as is the rising column of neutral material at  $l = 18^{\circ}$ .

a complex soap-bubble structure begins to fade into the emptiness of the shell. The void, where the top of the shell should be, is clearly seen throughout a large range of velocities. The high-latitude cloud peaks in column density at  $\sim +44 \text{ km s}^{-1}$ . It is on the extreme end of a vertical column of H I, extending away from the shell wall. The emission profiles for sight lines through this rising column show peak emission at  $+44 \text{ km s}^{-1}$ . The correlation between the velocity of the cloud centroid,  $+44 \text{ km s}^{-1}$ , and the front

and back sides of the shell itself, at  $+38$  and  $+68 \text{ km s}^{-1}$ , respectively, suggests that the vertical column and high-latitude cloud lie between the front and back sides of the shell. This connection is the first indication that the cloud is actually the ejecta of the Scutum shell, which has experienced “blowout.” We claim that hot material from the inside of the shell has been thrust beyond the disk of the Galaxy. The soap bubble structure around the shell, centered on  $l = 17^{\circ}5$ ,  $b = -4^{\circ}0$  and best seen at  $v = +38 \text{ km s}^{-1}$

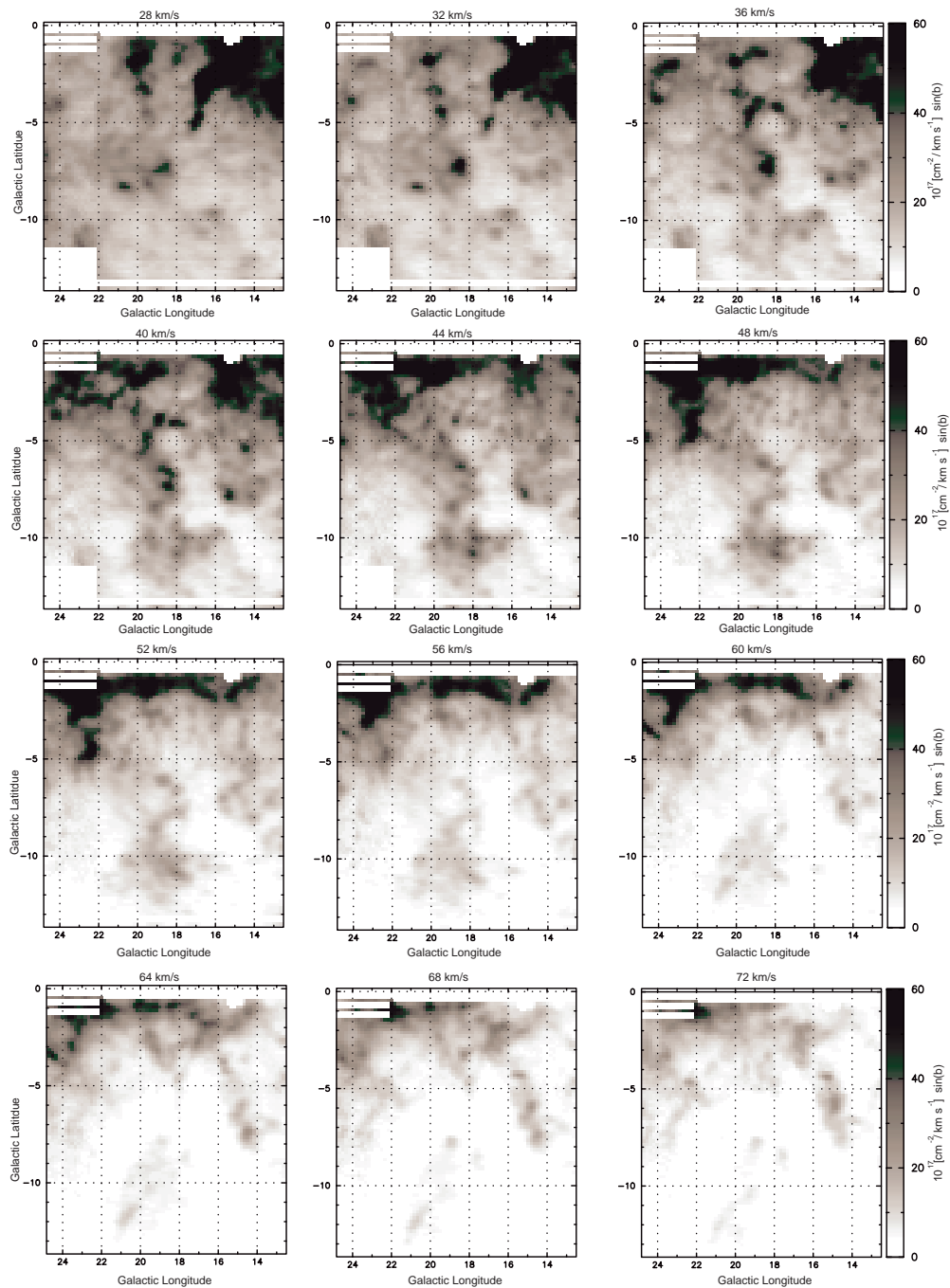


FIG. 3.—Evolution of the Scutum shell in velocity space. Individual frames of H I emission, each  $2 \text{ km s}^{-1}$  wide, in increments of  $4 \text{ km s}^{-1}$ , from the NRAO H I survey. To improve contrast, the column density has been multiplied by  $\sin |b|$ . Here we see the evolution of the Scutum shell in velocity space. The soap bubble structure of the ISM at  $\sim 36 \text{ km s}^{-1}$  opens into the Scutum shell at  $\sim +40 \text{ km s}^{-1}$ . The shell structure persists through the  $+52 \text{ km s}^{-1}$  region and then dissipates entirely by  $72 \text{ km s}^{-1}$ .

$\text{s}^{-1}$ , appears to be the near side of the shell. The far side of the shell is not easily seen in the H I images, but evidence for its existence is seen in the H I line profiles along several sight lines through the center of the shell. Figure 4 presents several H I velocity profiles from the region, highlighting the shell walls at  $+38$  and  $+68 \text{ km s}^{-1}$  at the middle latitudes and the rising column of H I at  $+44 \text{ km s}^{-1}$  seen at higher latitudes.

The complex morphology of the H I emission throughout the velocity range demonstrates the difficulty in determining concrete structural descriptions of the features. The

definitive statements that we can make based on the H I data are that there are columns of H I rising from the plane of the galaxy corresponding to GW 14.9–1.6, GW 16.9–3.8, and GW 19.5–6.4 in the Koo et al. (1992) catalog of IR emission structures. The walls surround a clear deficiency in H I emission, which has a roughly spherical shape. Furthermore, a vertical column of H I rises from this roughly spherical shell and culminates in a high-latitude cloud of neutral material. The velocities at which these features appear suggest a correlation between the high-latitude cloud and the low-latitude shell. We turn to

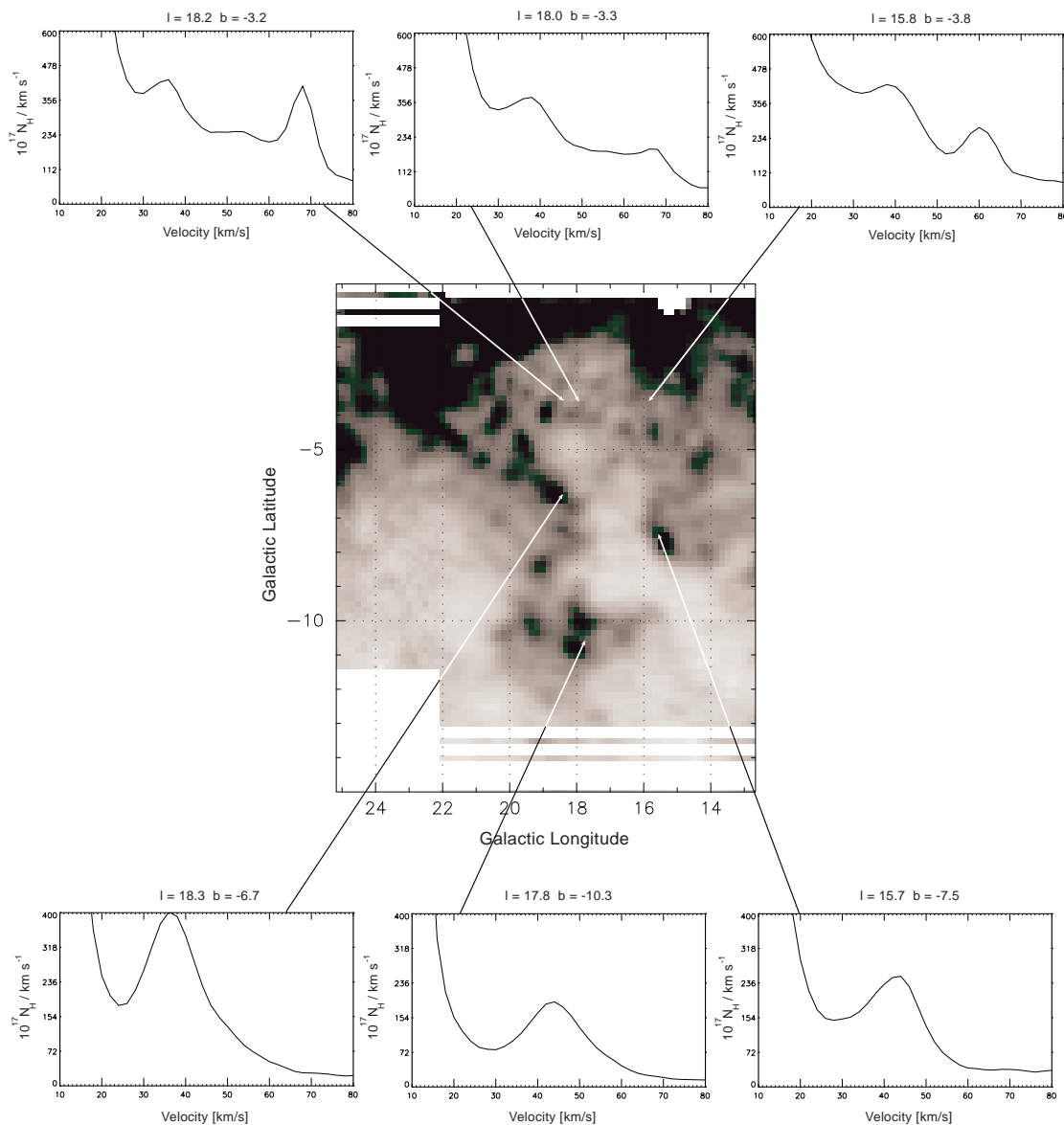


FIG. 4.—Scutum shell region with selected H I emission velocity profiles. Note the double-peaked profiles near the shell center, suggestive of front and back sides. The rising column and the high-latitude cloud occur at  $\sim +40$  km s $^{-1}$ , corresponding to the shell central velocity. This indicates a continuous structure of gas, rising from the top of the shell to high latitude.

other wavelengths to determine whether there is other evidence that connects these features.

### 3.2. Infrared Data

Infrared emission maps, with an angular resolution of  $6'.1$ , for the Scutum shell region have been obtained from the *IRAS* survey of Wheelock et al. (1991). The images were then modified via an unsharp mask technique to increase the contrast. In this process, the original image is divided by an image that is blurred over 25 pixels (about  $0'.3$ ). The four *IRAS* wavebands, 100, 60, 25 and 12  $\mu\text{m}$ , were examined for structures correlating to the H I emission, but notable features exist only in the 100 and 60  $\mu\text{m}$  wavebands. Figure 5 displays the 100 and 60  $\mu\text{m}$  infrared emission maps corresponding to the Scutum shell region. Correlations between these data sets and the H I data can be seen in the clumpy structures at  $l = 18'.5$ ,  $b = -6'.0$ . A decrease in IR emission can be seen in association with the shell center, surrounding  $l = 17'.5$ ,  $b = -4'.0$ , as well as within the missing shell top in

the H I image. It is notable that the clumps of bright *IRAS* emission in the 60 and 100  $\mu\text{m}$  images correspond with the location of bright 21 cm emission, indicating the presence of dust with the neutral material. This is especially noteworthy for the clumps at high latitudes,  $b \sim -10'$ , corresponding to the cloud of neutral H I, which we refer to as the high-latitude cloud.

### 3.3. X-Ray Data

X-ray data were taken from the *ROSAT* survey diffuse X-ray background maps of Snowden et al. (1995). These data were obtained with the Position Sensitive Proportional Counter (PSPC) of the *ROSAT* X-Ray Telescope (XRT). Exposure times and detected counts minus modeled background counts were accumulated into  $40' \times 40'$  pixels in two Aitoff equal-area, Galactic coordinate projections. The count map was divided by the exposure time map to produce a count-rate map. For the *ROSAT* XRT/PSPC instrument, X-ray energy information is divided into three

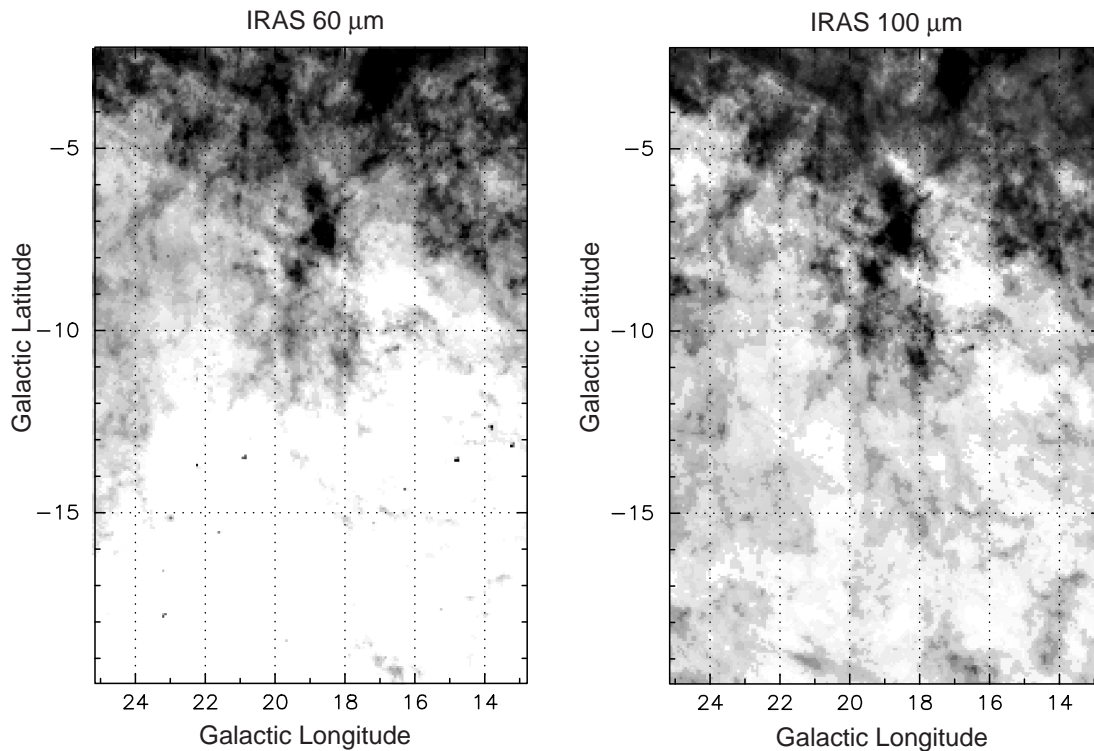


FIG. 5.—Unsharp-masked images of the Scutum shell region observed in *IRAS* 60 and 100  $\mu\text{m}$ . Note the clumpy structures at  $l = 18.5^\circ$ ,  $b = -6.5^\circ$  in the 60 and 100  $\mu\text{m}$  images. These are associated with the shell walls. At  $l = 18^\circ$  and  $b = 10^\circ$  we see clumps associated with the high-latitude cloud. The 100  $\mu\text{m}$  excess could be due to heating of the dust in the cloud from nearby O stars, or it could be indicative of a molecular component of the cloud with a column density as high as  $2.4 \times 10^{21} \text{ cm}^{-2}$ .

broad bands, resulting in overlapping instrumental response curves with mean energies near 0.25, 0.75, and 1.5 keV. We refer to maps for each of these energy bands. The data reduction techniques did not use the position information provided by the PSPC, and therefore the maps have an effective angular resolution  $\sim 2^\circ$ . More recent maps, produced using the full  $\sim 12'$  angular resolution of the PSPC, have been published by Snowden et al. (1997), but those data have not been made public.

Subsets of the described all-sky maps for a region of the sky covering  $l = 5^\circ$ – $25^\circ$  and  $b = 0^\circ$  to  $-20^\circ$  were extracted from the *ROSAT* public data catalog in the SkyView database located at NASA Goddard Space Flight Center. The data were linearly interpolated to produce smooth images and enhance morphological structure. The X-ray maps for the 0.25, 0.75, and 1.5 keV bands were then examined for their relation to the 21 cm emission in the Scutum shell region. This region was defined as  $l = 12^\circ$ – $25^\circ$  and  $b = 0^\circ$  to  $-20^\circ$ . Sections of the X-ray emission maps of this region were overlaid with the H I images to compare morphology. In overlaying the images, the X-ray data were smoothed using nearest neighbor sampling. There is no velocity resolution in the X-ray data, so we examine the entire velocity range of the H I data to find where the X-ray contours best correlate to observed features. Our goal is to determine whether the observed X-ray emission can be associated with the 21 cm emission.

### 3.3.1. The X-Ray Absorption Correction

Foreground H I strongly attenuates the X-ray emission in each of the three bands. To determine whether the morpho-

logical features seen in X-ray emission are associated with the Scutum Supershell, we attempt to remove the effects of this absorption. X-ray emission attenuates according to the optical depth  $\tau$ , which depends upon the column density of the absorbing medium and the energy of the X-rays. In addition, each *ROSAT* energy channel has a finite width. Thus, we must use an effective optical depth  $\tau_{\text{eff}}$  that reflects instrumental sensitivity over a given energy band weighted by the emitting X-ray spectrum. Since each of the *ROSAT* all-sky maps includes a broad band of energies, we do not have spectral information. Therefore, we are forced to assume a gas temperature, which determines a model X-ray spectral shape. The observed total H I column density for each pixel of the NRAO H I map, together with the assumed X-ray spectral shape, determines  $\tau_{\text{eff}}$ . Figure 6 displays the H I column density velocity plane map at  $+44 \text{ km s}^{-1}$  alongside the observed X-ray data.

The model spectrum was produced using the Raymond & Smith (1977) model of X-ray emission within the XSPEC software package (Arnaud 1996). The model emission requires as inputs an H I column density and an assumed temperature. The model then outputs a count rate for eight energy channels, corrected by the *ROSAT* response matrix. The channels corresponding to 0.25, 0.75, and 1.5 keV bands were binned to yield the total model-predicted count rate for X-rays in those energy bands. For a range of H I column densities and temperatures, we then calculate the ratio of count rate for a given absorbing column to that of zero absorbing column to give an effective optical depth. In this manner, a grid of effective optical depth  $\tau_{\text{eff}}$  as a function of H I column density and temperature was produced.

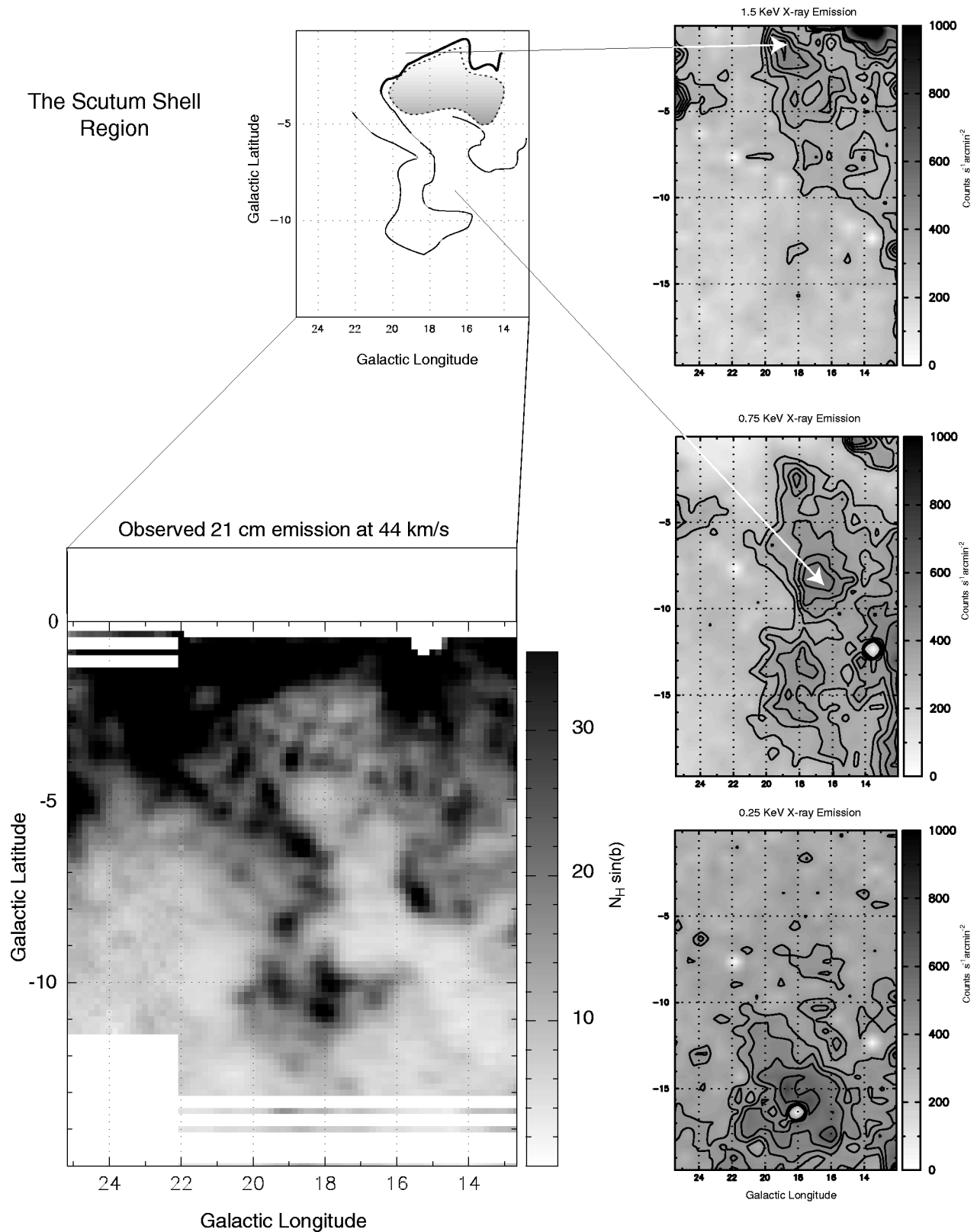


FIG. 6.—Observed *ROSAT* X-ray emission together with the NRAO  $+44 \pm 1 \text{ km s}^{-1}$  H I velocity plane. It is notable that the X-ray morphologies of each band anticorrelate with the 21 cm emission. It is also apparent that emission peaks in the 1.5 keV emission overlap the 0.75 keV, and the 0.75 keV peaks then overlap with the 0.25 keV, suggesting a continuous distribution of hot gas. The 1.5 keV emission is located at the base of the Scutum shell and corresponds to the location of the S55 H II region and the O7 star HD 171198.

The X-ray emission model and the resultant fitting functions are presented in the Appendix.

The total H I column density was calculated for each pixel of the NRAO H I survey, and the effective optical

depth was then interpolated from the grid of  $\tau_{\text{eff}}$  values for each pixel of the X-ray maps. It is impossible to determine how much of the observed H I lies on the near side of the Galactic rotation curve, between the Sun and the Scutum

shell, so the total column density over the entire velocity range was used as a worst-case scenario, assuming that all of the observed H I lies between the Sun and the X-ray-emitting region. Using the total column density calculated from the H I emission maps, a temperature was assumed for each X-ray band to produce the model X-ray emission. The assumed values of  $\log T$  were 7.0, 7.0, and 6.5 for the 1.5, 0.75, and 0.25 keV bands, respectively. Maximum X-ray counts for the model spectrum are found to occur near  $\log T = 7.0$  for the 0.75 and 1.5 keV X-rays, while the 0.25 keV X-rays maximized near  $\log T = 6.5$ . In addition, these temperatures were found to best preserve the morphology of the observed X-ray features. The choice of these temperatures will be further discussed in the Appendix.

For the 0.25 keV X-rays, the emission becomes less obscured at higher latitudes, beyond the limits of the NRAO survey. For this case, we turned to the H I 21 cm data of Hartmann & Burton (1997, hereafter HB). The HB survey was obtained at the Dwingeloo 25 m telescope and covers the entire sky at declination greater than  $-30^\circ$ . These data have a resolution of  $30'$ , compared to the  $21'$  of the NRAO survey. Details may be found in the Atlas of Galactic Neutral Hydrogen (Hartmann & Burton 1997). We extracted a region of the total H I column density map of the HB survey corresponding to the Scutum shell region. This column density map provides a second measure of the intervening H I column density, with greater coverage in Galactic latitude. With  $N_{\text{H}}$  and temperature  $T$  given for each pixel of the X-ray maps,  $\tau_{\text{eff}}$  is determined for each pixel.

Before applying  $e_{\text{eff}}^{\tau}$  to correct for X-ray absorption, we attempt to correct for a uniform foreground X-ray emission. We are interested only in the enhancement features associated with the Scutum shell region. Therefore, we calculate the average X-ray counts in a field away from these features. In this manner, we estimate the emission that may be associated with any local hot gas or emission unrelated to the Scutum enhancements. After this subtraction is made, we correct for absorption due to the intervening H I. The corrected count rate for the Scutum X-ray enhancement may be expressed as

$$I = (I_{\text{observed}} - I_{\text{baseline}})e_{\text{eff}}^{\tau}. \quad (1)$$

This method is explained more fully in § 5.3. The observed and absorption corrected X-ray emission maps are presented in Figure 7.

The removal of the X-ray emission from the foreground gas is a very uncertain step in the correction process. In the maps of Figure 7 at 0.75 and 0.25 keV, for directions close to the Galactic plane ( $|b| < 2^\circ$ ), where the X-ray absorption is extremely large, this foreground correction has resulted in the unrealistic elimination of most of the X-ray emission in the corrected maps. The uncertainties in the corrected results displayed in Figure 7 increase very significantly as  $|b|$  decreases.

### 3.3.2. Qualitative Aspects of the X-Ray Features

Conspicuous anticorrelation between the X-ray and 21 cm emission can be identified in the  $+44 \text{ km s}^{-1}$  velocity plane. At this velocity, each of the X-ray images displays features that indicate a connection with the Scutum shell. Figure 6 shows the observed (uncorrected) X-ray emission with the  $+44 \text{ km s}^{-1}$  velocity plane of the NRAO H I

survey. The 1.5 keV emission resides at the base of the Scutum shell close to the Galactic plane, the 0.75 keV X-ray contours fit the interior of the shell as well as the void seen in the H I above the shell, and the 0.25 keV emission resides above the high-latitude cloud. With such a coincidence, the presence of X-rays in the Scutum shell region is most likely indicative of hot gas created by some energetic phenomena that formed the H I structures.

The 1.5 keV X-ray emission, corresponding to the base of the Scutum shell, peaks near the shell's central region. The uncorrected emission map shows a definite conelike shape, originating at  $l = 20^\circ$  and  $b = -1^\circ$ , indicating a prominent region of hot gas extending into the shell. The absorption corrected maps seen in Figure 7 show a hemispherical bulge protruding into the Scutum shell. The 1.5 keV X-ray emission maps also display evidence of limb brightening, which is most clearly seen in the maps corrected by the HB survey, at  $l = 16^\circ$  and  $18^\circ$  and  $b \sim -3^\circ$  to  $-5^\circ$ . This limb brightening is also seen in the 0.75 keV map at the same position. Our calculations assume all of the observed H I lies in the foreground and thus overcorrects the emission. It may therefore be expected that the 21 cm morphology be imposed upon the X-ray data. The absorption correction would then be expected to smooth the X-ray enhancement features, brightening regions where 21 cm emission is strong. However, it remains clear that the X-ray emission anticorrelates to the H I 21 cm emission, even in the absorption-corrected emission maps, suggesting that the enhancement features are real and not artifacts of absorption. The limb brightening that occurs between  $l = 16^\circ$  and  $18^\circ$  is just inside the walls of the 21 cm emission.

In both the observed and absorption corrected emission maps, the 0.75 keV emission exhibits peak values at locations similar to the 1.5 keV bright spots. The 0.75 keV emission displays a similar conelike structure near the plane, which culminates in a bright patch just above the blown-out top of the shell, at  $l = 17^\circ$ ,  $b = -8^\circ$ . A second bright patch appears at even higher latitudes,  $b = -13^\circ$ , corresponding to the peak 0.25 keV emission. Limb brightening features of the absorption corrected 0.75 keV X-rays are seen at  $l = 17.8$  and  $b = -3.3$ , corresponding nicely with the centroid of the supershell, while peak values occur above and below this region, at  $l = 17^\circ$ ,  $b = -8^\circ$ , and  $l = 18^\circ$ ,  $b = -2^\circ$ . The X-ray emission above the shell corresponds to the empty gap in H I emission above the shell, culminating just below the high-latitude cloud. This peak is located just above the void where the top of the shell would be. The mid-latitude feature is seen clearly in the HB corrected 0.75 keV map. The low-latitude features display strong limb brightening, with peak emission again just inside the walls of cool 21 cm emission. The two peaks in 0.75 keV emission lie within the shell itself, corresponding to the hot contents of the shell, and above the shell, associated with escaping gas.

At high latitude, where H I column density is low, we see strong emission from 0.25 keV X-rays in the uncorrected X-ray maps. The first traces of the 0.25 keV X-rays are seen in the region above the blown out top of the shell, between  $l = 16^\circ$  to  $18^\circ$  and  $b = -6^\circ$  to  $-8^\circ$ , coinciding with the fading 0.75 keV X-rays. The 0.25 keV emission continues to higher latitude with a peak at  $-15^\circ$ . Assuming this hot gas originated in the Scutum shell, at a distance of 3.3 kpc, the 0.25 keV emitting gas then lies at a vertical distance of  $\sim 850$  kpc from the Galactic plane. However, the correction

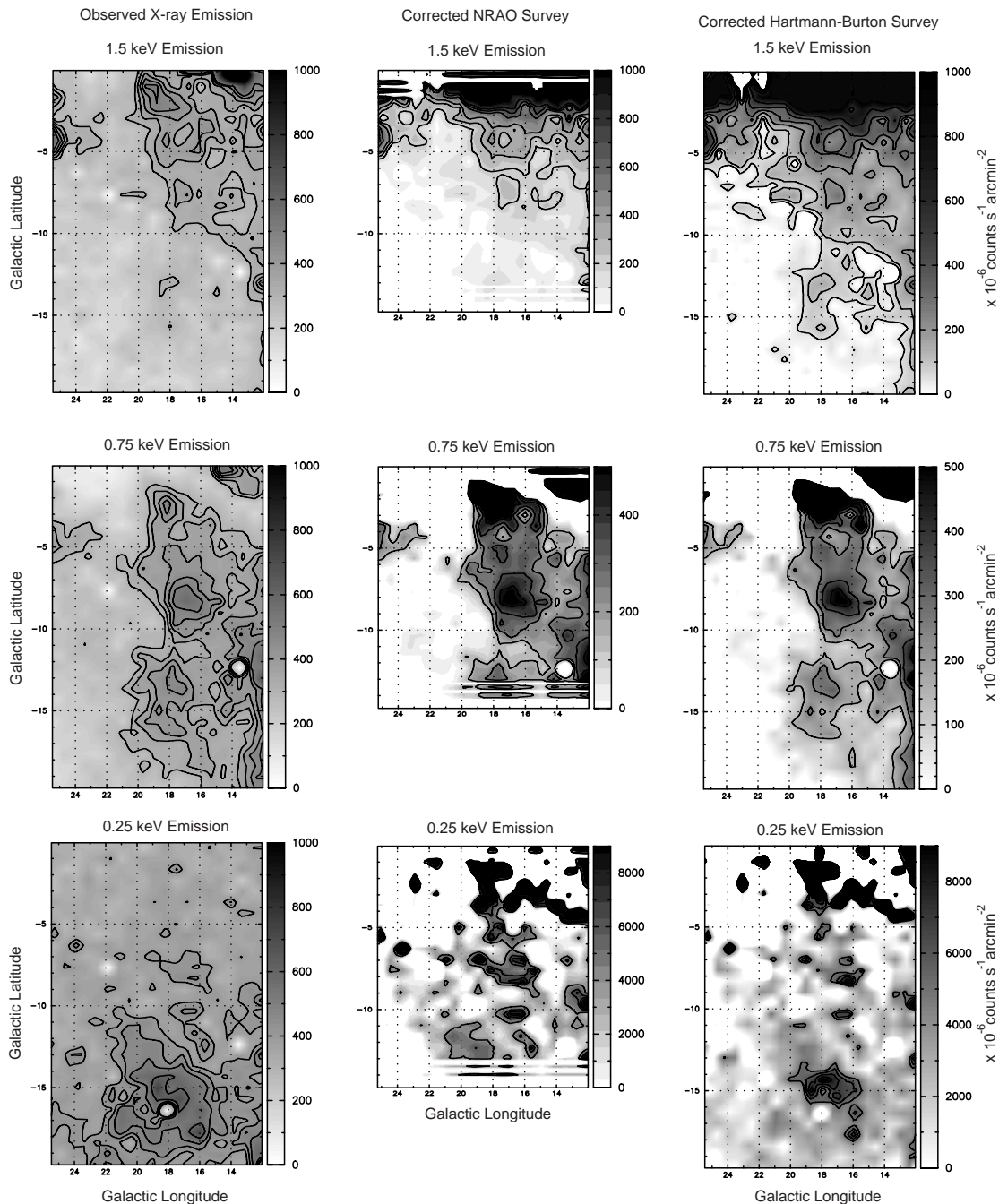


FIG. 7.—Observed X-ray emission from *ROSAT* (1995) together with the maps corrected for local emission and foreground absorption. The three bands, 1.5, 0.75, and 0.25 keV, display morphological features that connect it with the Scutum shell. Hot gas within the shell and near its base emits 1.5 keV X-rays, which dissipate near the blown-out top of the shell, becoming 0.75 keV and, finally, 0.25 keV at high latitudes.

factor for absorption is particularly large with the 0.25 keV X-rays. Thus the corrected emission map loses much of the morphological characteristics seen in the original map. However, even after the absorption correction, the enhancement at  $b = -14^\circ$  remains at 56% over baseline levels, and closely correlates to a similar feature in the 0.75 keV X-rays at the same latitude. These corrections indicate that the 0.25 keV X-ray emission is still a significant enhancement even at high latitudes. This enhancement corresponds to  $10^6$  K gas at  $\sim 850$  pc from the plane of the Galaxy.

In summary, the anticorrelation between the X-rays and the 21 cm emission is quite pronounced, indicating that the

hot gas responsible for the X-ray emission lies at the distance associated with the Scutum shell region. This implies the presence of hot gas within and above the Scutum shell. The emission in the 0.25 keV and 0.75 keV X-ray bands seems to be clearly related to the same hot material. While the 0.25 keV emission suffers greatly from absorption due to foreground material, the enhancement is still present after the correction. The absorption correction is a worst-case scenario for absorption, as we assume that all of the observed H I is foreground material. Thus, it is likely that the 0.25 keV enhancement feature is real and related to the enhancement seen in the 0.75 keV and 1.5 keV bands.

### 3.4. H $\alpha$ Data

The portion of the sky corresponding to the Scutum shell was observed with the Wisconsin H-Alpha Mapper (WHAM) during its all sky H $\alpha$  survey. The WHAM instrument is a 0.6 m all-sky siderostat connected to a 15 cm double-etalon Fabry-Perot spectrometer, which delivers a spectrum covering a  $200 \text{ km s}^{-1}$  radial velocity interval from a  $1^\circ$  circular patch on the sky. For the survey, the  $1^\circ$  diameter beam of the WHAM instrument is centered on a  $0.98^\circ \times 0.85^\circ$  grid in Galactic longitude and latitude. Each  $1^\circ$  pixel has an integration time of 30 s, a signal-to-noise ratio of about 30 in baseline continuum regions of the spectrum, and a spectral resolution of  $12 \text{ km s}^{-1}$ . Detailed descrip-

tions of the WHAM instrument and survey may be found in Tufté (1997) and Haffner (1999). To compare the morphological features seen in H I to those seen in H $\alpha$ , we extracted the region of the WHAM survey corresponding to the Scutum shell. Figure 8 displays these maps for the range of LSR velocities from 0 to  $+80 \text{ km s}^{-1}$ . Figure 9 focuses on the  $+40 \text{ km s}^{-1}$  emission map and includes significant H $\alpha$  emission profiles.

As with the X-ray data analyzed in § 3.3.1, foreground absorption is again a factor in analyzing the H $\alpha$  emission. Corrections were performed by averaging the H I column density over  $1^\circ$  square portions of the HB H I survey. Average column density is then converted to an average extinction  $E(B-V)$  for these  $1^\circ$  patches according to the

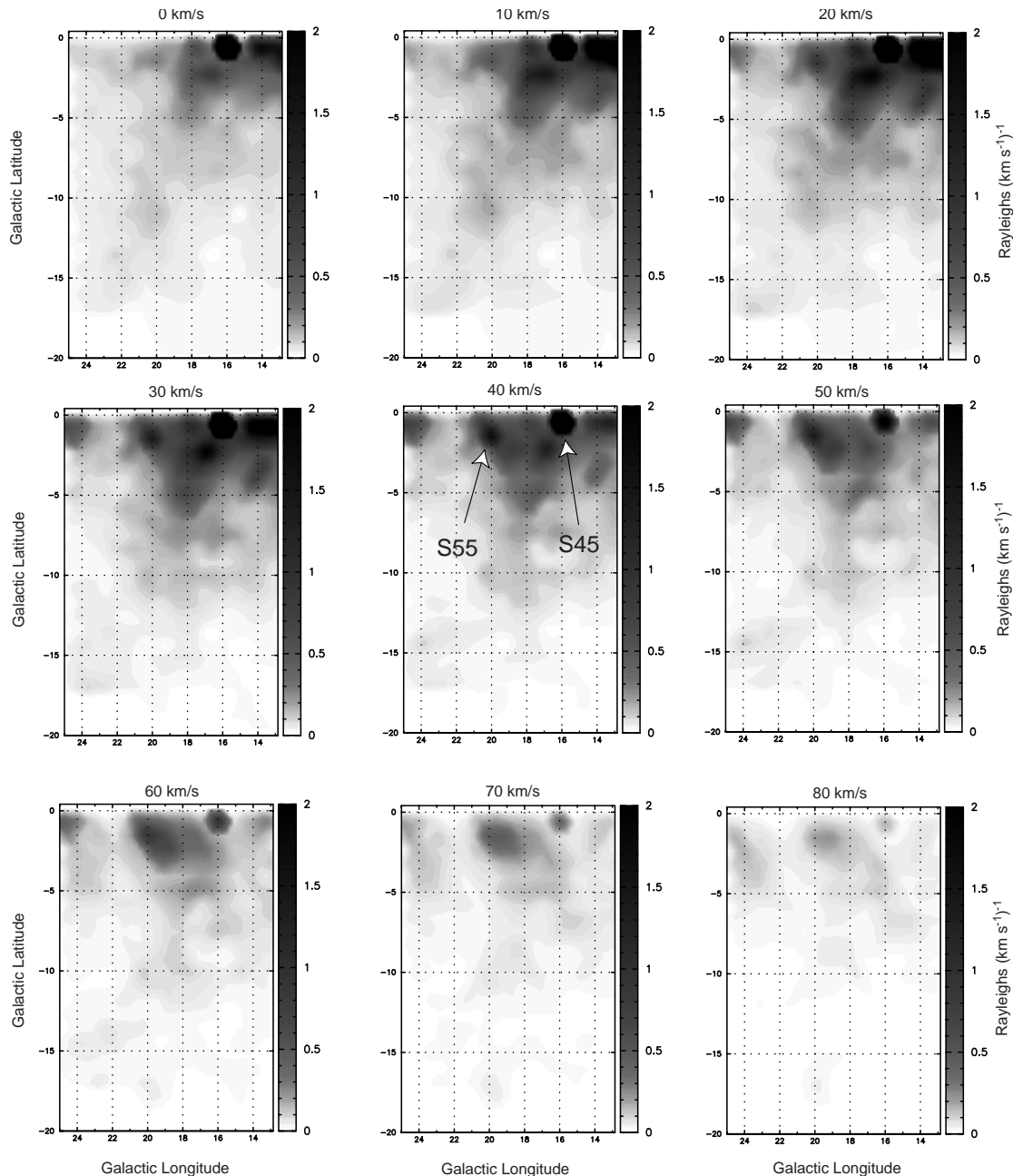


FIG. 8.—Evolution of H $\alpha$  emission in velocity space. Individual frames of the WHAM H $\alpha$  survey in Rayleighs  $(\text{km s}^{-1})^{-1}$ . Each frame is  $10 \text{ km s}^{-1}$  wide, in  $10 \text{ km s}^{-1}$  increments, displaying the evolution of the H $\alpha$  emission through velocity space. Note the primary H II regions S45 and S55 in the  $+40 \text{ km s}^{-1}$  LSR velocity plane. These are the major contributors to the region of H $\alpha$  emission enhancement seen at the base of the Scutum shell region.

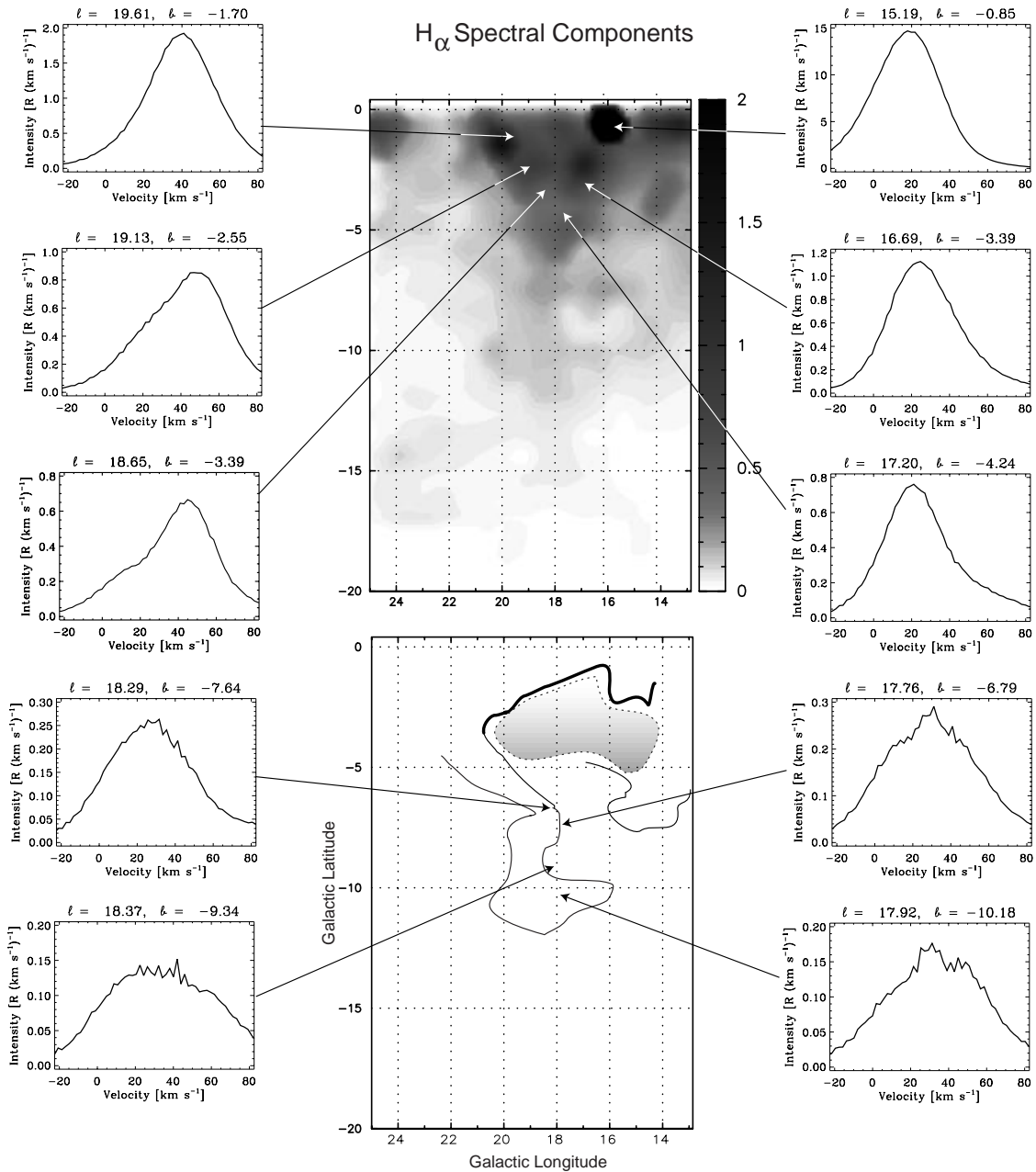


FIG. 9.—WHAM  $H\alpha$  survey in the  $+40 \pm 5 \text{ km s}^{-1}$  LSR velocity plane. Selected profiles are included, demonstrating that peak  $H\alpha$  emission occurs in two components. The first component peaks at  $+20 \text{ km s}^{-1}$ , corresponding to the S45 H II region; the second component peaks at  $+40 \text{ km s}^{-1}$ , corresponding to the S55 H II region. The vertical column of  $H\alpha$  emission has two Gaussian components, producing the broad peak at  $+30 \text{ km s}^{-1}$ . The primary Gaussian component is that at  $+40 \text{ km s}^{-1}$ , the same kinematic distance as the analogous H I column. This demonstrates the presence of ionized material within the Scutum shell and extending to latitudes  $\sim -12^\circ$ .

value  $\langle N(\text{H I})/E(B-V) \rangle = 4.93 \times 10^{21} \text{ cm}^{-2} \text{ mag}^{-1}$  found by Diplax & Savage (1994). The extinction curve of Cardelli, Clayton, & Mathis (1989) provides the extinction optical depth,  $\tau$ , at  $H\alpha$  as a function of H I column density. Again we use a worst-case scenario, assuming the entire H I column is foreground material. This absorption correction ignores the contributions to the observed emission produced by dust scattering radiation into the line of sight.

#### 3.4.1. Qualitative Aspects of the $H\alpha$ Features

Notable features occurring in the  $+40 \text{ km s}^{-1}$  LSR velocity plane include a hemispherical bulge at the base of the Scutum shell and a rising column of emission extending

to higher latitudes. Correlations between the  $H\alpha$  and the H I emission are evident in these features. The low-latitude, hemispherical  $H\alpha$  emission traces the shape of the Scutum shell, and the vertical column of H I seen in the 21 cm data corresponds to the similar feature seen in the  $H\alpha$ , which culminates in a similar high-latitude cloud. The correlations are somewhat uncertain because of the difference in velocity resolution. The observed  $H\alpha$  line width, because of thermal and nonthermal motions, is larger than  $10 \text{ km s}^{-1}$ . Thus detailed information regarding the velocity structure of the Scutum shell is less obvious. However, the correlations seen in the emission maps can still be studied further with velocity profiles along selected sight lines.  $H\alpha$  emission spectra may be examined for particular Gaussian components. We

find a component at  $+44 \text{ km s}^{-1}$  that corresponds to the Scutum shell.

The hemispherical bulge in the  $+40 \text{ km s}^{-1} \text{ H}\alpha$  emission map lying at the base of the Scutum shell shows prominent emission enhancements at  $l = 16^\circ$ ,  $b = -1^\circ$ ; and  $l = 20^\circ$ ,  $b = -1^\circ$ . These enhancements correspond to discrete H II regions. Table 1 indicates H II regions from the catalog of Lockman (1989) in the longitude region of the Scutum shell. For his survey, H II regions were detected via the radio recombination line emission. We examine velocity profiles of H $\alpha$  emission to verify which of the bright H $\alpha$ -emitting H II regions lie at the kinematic distance associated with the Scutum shell. There are a total of 90 H II regions between  $l = 14^\circ$  and  $25^\circ$ . Of these, 11 have velocities between  $+40$  and  $+50 \text{ km s}^{-1}$ . In addition, the survey of H II regions of Blitz et al. (1982) add a small number of H II regions away from the Galactic plane, beyond the limits of the Lockman (1989) survey. Specifically, the regions S50, S51, and S55, named for their entries in the Sharpless catalog, lie at  $b < -1^\circ$ .

H $\alpha$  emission profiles through the Scutum region reflect two dominant emission regions at  $+20 \text{ km s}^{-1}$  and  $+40 \text{ km s}^{-1}$ , with the emission peaks blending to form a wide feature at  $+30 \text{ km s}^{-1}$  at high latitudes. The region of emission at  $+40 \text{ km s}^{-1}$  may then be associated with the H II regions in this velocity range. Images in Figure 9 display the region in H $\alpha$  emission with selected emission profiles.

A strong peak in H $\alpha$  emission near  $l = 20^\circ$ ,  $b = -1^\circ$ , is very close to the peak  $1.5 \text{ keV}$  X-ray emission (Fig. 7). The H $\alpha$  emission morphology of this feature and the uncorrected  $1.5 \text{ keV}$  X-ray emission morphology share conspicuous similarities. Both features have a cone like shape, opening into the Scutum shell, suggesting that the emitting gas flows directly into the shell. The H II region S55 lies at this position as well. The CO survey of Dame et al. (1986) indicates the presence of a molecular cloud just below this hot region of the Scutum shell, at  $l = 20^\circ$  in the Galactic plane. It appears that the  $l = 20^\circ$  region involves a layer of molecular material in the plane of the Galaxy, above which is a warm region corresponding to the S55 H II region and a hot region corresponding to the  $1.5 \text{ keV}$  X-ray emission.

The rising column of H $\alpha$  emission seen in the  $+40 \text{ km s}^{-1}$  emission map closely correlates to the vertical column of H I seen in the  $+44 \text{ km s}^{-1}$  velocity plane. The morphology of this cloud is strikingly similar to the high-latitude cloud of neutral material. The H $\alpha$  emission component peaks at  $+40 \text{ km s}^{-1}$ , placing it at the kinematic distance

indicated by the centroid of the neutral emission. Moreover, the profiles along sight lines with increasing latitude display a decrease in H $\alpha$  intensity.

### 3.5. Ultraviolet Data

During its 18 yr lifetime, the *International Ultraviolet Explorer (IUE)* satellite obtained high-dispersion UV spectra of a large number of O and B stars, including many in the general direction of the Scutum Supershell and its high-latitude cloud. Of particular interest are those distant stars that can be used to investigate the UV absorption properties of the supershell. Close to the Galactic plane, in the direction  $l = 15^\circ$ – $20^\circ$ , the extinction is very large for objects distant enough to be associated with the supershell ( $d > 3 \text{ kpc}$ ). Therefore, high-dispersion UV observations are difficult to obtain for low-latitude stars possibly associated with the supershell. However, there are several distant stars in the *IUE* high-dispersion archive that permit a study of the gas associated with the high-latitude ejecta of the supershell in directions with  $b = -10^\circ$  to  $-12^\circ$ .

Table 3 lists properties of three stars for which high-quality *IUE* high-dispersion spectra exist. Two of the stars (HD 175754 and HD 175876) may actually be physically associated with the higher latitude cloud. The third star (HD 177989) is a more distant inner Galaxy star in a direction that passes through the higher latitude cloud. All three stars lie in directions for which there is detectable H I emission from gas associated with the high-latitude cloud (see Figs. 2 and 12). The H I emission is strongest for the directions to HD 177989 and HD 175754.

HD 175754 (O8 IIf) and HD 175876 (O 6.5 IIIInf) are both very interesting O stars. With line-of-sight distances of 2.75 and 2.35 kpc, respectively, these two O stars lie 0.47 and 0.43 kpc below the Galactic plane. The close proximity of HD 175754 and HD 175876 to the direction of the unusual high-latitude cloud above the Scutum Supershell may indicate either that these O stars were formed in a cloud being ejected from the Galactic plane or that they may have recently formed at their current  $z$  distances.

High dispersion *IUE* echelle spectra obtained with the short wavelength prime (SWP) camera of the three stars listed in Table 3 were taken from the *IUE* data archives. We chose to work with the originally extracted spectra (version 1.0 of the *IUE* spectral extraction software for HD 175754 and HD 175876 and version 2.0 for HD 177989) rather than the newly extracted spectra (*IUE* NEWSIPS MXHI) because of the serious systematic problems associated with

TABLE 3  
PROPERTIES OF THE STARS OBSERVED WITH *IUE*<sup>a</sup>

HD	MK	$V$ (mag)	$E(B-V)$ (mag)	$l$ (deg)	$b$ (deg)	$d$ (pc)	$z$ (pc)	$v \sin i$ ( $\text{km s}^{-1}$ )	$\log N(\text{H I})$ ( $\text{cm}^{-2}$ )
175754.....	O8 IIf	7.01	0.23	16.40	-9.92	2750	-470	176	21.04
175876.....	O6.5 IIIInf	6.94	0.22	15.28	-10.58	2350	-430	292	21.04
177989.....	B0 III	9.33	0.25	17.82	-11.88	4910	-1010	150	20.95

<sup>a</sup> The entries in this table are from Diplás & Savage 1994 and references therein, except for the values of the rotational velocity,  $v \sin i$ , which are from Penny 1996 for HD 175754 and HD 175876 and from Savage & Massa 1987 for HD 177989. The distance estimates are from the method of spectroscopic parallax (see Diplás & Savage 1994 for details). The stars are too distant for *Hipparcos* parallax measurements to be useful. Note that the distances for HD 175754 and HD 175876 listed here differ somewhat from those adopted in the Garmany et al. 1982 O star catalog and listed in Table 2. The following *IUE* SWP spectra were combined for each of the three stars: HD 175754 (SWP 09320, 02813, 04901, 13591, 13728, 14803); HD 175876 (SWP 09321, 10025); and HD 177989 (SWP 23867, 36325, 36326, 36333). The values of  $v_{\text{LSR}} - v_{\text{HELIO}}$  used in the processing for HD 175754, HD 175876, and HD 177989 are  $+10.6$ ,  $+10.4$ , and  $+10.5 \text{ km s}^{-1}$ , respectively.

the new *IUE* high-dispersion extraction method (Massa et al. 1998). For each of the three stars the multiple SWP spectra were aligned in velocity and co-added following the detailed procedures discussed by Sembach & Savage (1992). The actual *IUE* SWP spectra utilized in our analysis are listed in the footnotes of Table 3 along with the values of  $v_{\text{LSR}} - v_{\odot}$  toward each star. We estimate the spectral resolution (FWHM) of the co-added spectra to be  $30 \text{ km s}^{-1}$  for HD 175754 and HD 175876 and  $25 \text{ km s}^{-1}$  for HD 177989.

Plots on an LSR velocity basis of various interstellar absorption lines seen toward each star are illustrated in Figure 10. The absorption lines, illustrated from top to bottom, include a stellar photospheric line Si III\*  $\lambda 1294.54$  and the following ISM lines: Si II  $\lambda 1808.01$ , Si II  $\lambda 1260.42$ , Si III  $\lambda 1206.50$ , Al III  $\lambda 1862.79$ , Al III  $\lambda 1854.72$ , Si IV  $\lambda 1402.77$ , Si IV  $\lambda 1393.76$ , C IV  $\lambda 1550.77$ , C IV  $\lambda 1548.20$ , N V  $\lambda 1242.80$ , and N V  $\lambda 1238.82$ . More than one interstellar species appears in absorption for some of the velocity regions plotted in Figure 10. S II  $\lambda 1259.52$  is present at  $-215 \text{ km s}^{-1}$  in the Si II  $\lambda 1260.42$  spectra. S I  $\lambda 1807.31$  appears at  $-116 \text{ km s}^{-1}$  in the Si II  $\lambda 1808.01$  spectra. Mg II  $\lambda \lambda 1239.93$  and  $1240.39$  appear at  $+269$  and  $+380 \text{ km s}^{-1}$  in the N V

$\lambda 1238.82$  panels. The location of prominent detector registration marks (reseau) are listed in the figure caption. The stellar photosphere Si III\*  $1294.54 \text{ \AA}$  line at the top of each panel can be used to judge the stellar blending problems that might be associated with each star. In all three cases the stellar rotational velocity is relatively large (see Table 3), so stellar blending is not a serious problem.

We note that *IUE* UV absorption line spectra for HD 175754 and HD 177989 have already appeared in the literature. Pottasch, Wesselius, & Arnal (1980) reported results on abundances and physical conditions in an intermediate negative-velocity cloud at  $v_{\text{LSR}} = -75.5 \text{ km s}^{-1}$  seen in the spectrum of HD 175754. They found the elemental abundances to be closer to solar than for typical diffuse interstellar clouds. This is probably the result of shock processing of the grains in the cloud and the return of those elements to the gas phase by whatever process accelerated the cloud to its observed velocity. In the direction to HD 175754, the effects of Galactic rotation produce increasing positive velocity with increasing distance to the star. Therefore, the actual speed of this intermediate negative velocity gas with respect to its surrounding environment probably substantially exceeds  $76 \text{ km s}^{-1}$ . Sembach & Savage (1992)

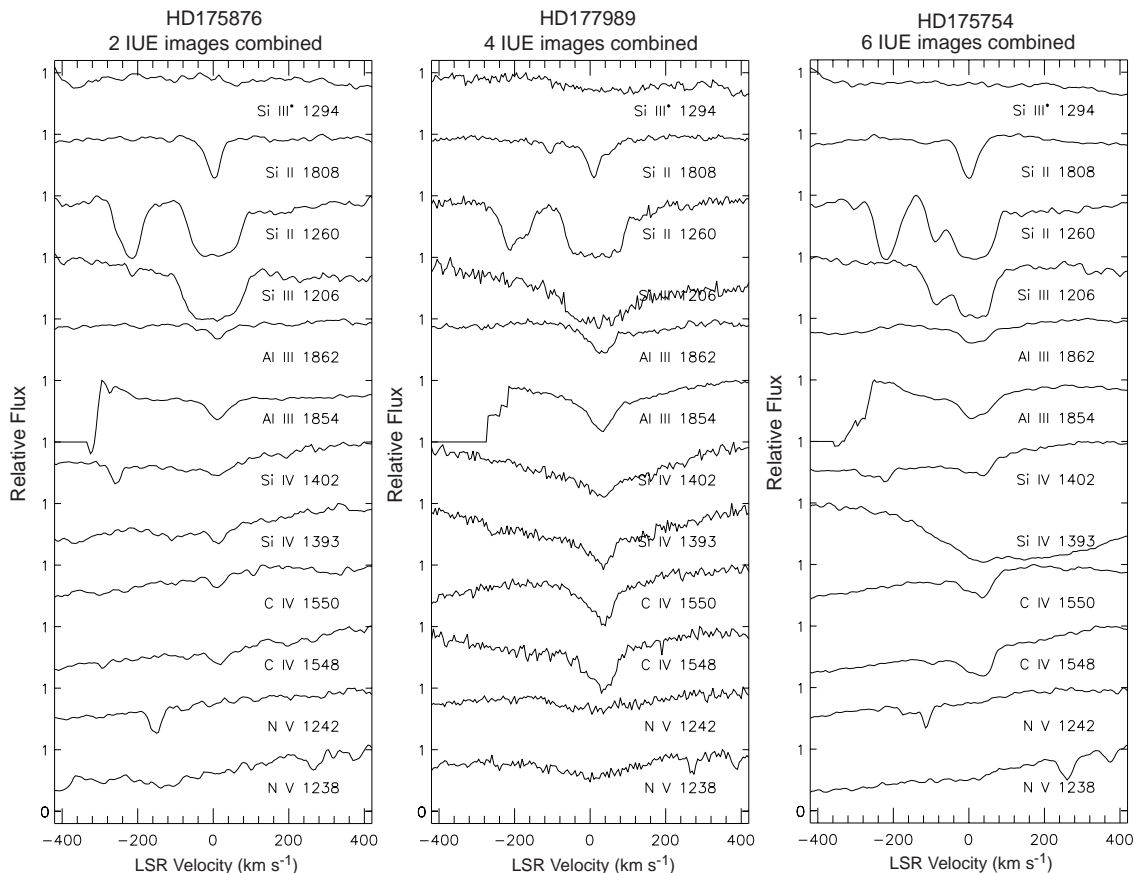


FIG. 10.—Relative intensity vs. LSR velocity ( $\text{km s}^{-1}$ ) for a selected set of interstellar lines in *IUE* spectra for three stars in the general direction of the high-latitude cloud above the Scutum Supershell. The zero level for each spectral region is at the tick level immediately below each spectrum. The spectra were obtained by combining 2, 4, and 6 individual *IUE* high-dispersion echelle spectra. The ISM lines shown are indicated just below each  $\pm 400 \text{ km s}^{-1}$  region of the spectrum illustrated. The line displayed at the top of each panel, Si III\*  $\lambda 1294.54$ , arises in the stellar photosphere and can be used to gain information about possible complications due to stellar line blending. In some of the panels, more than one species produces absorption over the velocity range illustrated. S II  $\lambda 1259.52$  is present at  $-215 \text{ km s}^{-1}$  in the Si II  $\lambda 1260.42$  spectra. S I  $\lambda 1807.31$  appears at  $-116 \text{ km s}^{-1}$  in the Si II  $\lambda 1808.01$  spectra. Mg II  $\lambda \lambda 1239.93$  and  $1240.39$  appear at  $+269$  and  $+380 \text{ km s}^{-1}$  in the N V  $\lambda 1238.82$  panels. Prominent detector registration marks (reseau) occur at  $\sim -120$  to  $-160 \text{ km s}^{-1}$  in the N V  $\lambda 1242.80$  panels and at  $\sim -220$  to  $-260 \text{ km s}^{-1}$  in the Si IV  $\lambda 1402.77$  panels. The spectra for HD 175754 and HD 175876 were processed with an early version of *IUE* processing software and therefore have a somewhat poorer velocity resolution than the observations for HD 177989 ( $30$  versus  $25 \text{ km s}^{-1}$  FWHM, respectively).

included HD 177989 as part of their study of highly ionized gas in the Milky Way disk and halo. They noted the extreme strength of the absorption produced by highly ionized gas atoms along this site line, particularly near  $v_{\text{LSR}} \sim +30$  to  $+40$  km s $^{-1}$  (see their Fig. 6).

In the following discussion we will concentrate on the absorption properties of the highly ionized gas toward the three stars listed in Table 3 whose spectra are shown in Figure 10. All three stars have relatively smooth stellar continua in the vicinity of the important C iv  $\lambda\lambda 1548.20$ ,  $1550.77$  doublet. In the case of HD 177989 the large  $v \sin i$  provides a smooth continuum. For the two O stars, HD 175754 and HD 175876, the interstellar C iv lines lie on the very smooth and broad C iv P-Cygni profiles.

Figure 11 shows continuum normalized line profiles of the C iv doublet on an expanded LSR velocity scale for each of the three stars. The C iv interstellar absorption is weak for the sight line to HD 175876, strong for HD 175754, and extremely strong for HD 177989. The C iv interstellar absorption, even at the relatively low resolution of the *IUE*, reveals a component structure. HD 175876 has a relatively weak component at  $v_{\text{LSR}} = +20$  km s $^{-1}$  and no absorption at higher positive velocities. HD 175754 has a weak component at  $v_{\text{LSR}} = +20$  km s $^{-1}$  and a strong component at  $v_{\text{LSR}} = +40$  km s $^{-1}$ . HD 177989 has a weak component at  $v_{\text{LSR}} = +20$  km s $^{-1}$  and extremely strong component at  $v_{\text{LSR}} = +40$  km s $^{-1}$ .

A reasonable interpretation for the absorption along the line of sight to these three stars is that the path to HD 175876 samples C iv absorption associated with the Sagittarius spiral arm at  $v_{\text{LSR}} = +20$  km s $^{-1}$  while the paths to HD 175754 and HD 177989 have additional contributions associated with gas at  $v_{\text{LSR}} = +40$  km s $^{-1}$  overlying the Scutum Supershell. If the stellar distances listed in Table 3 are correct, the absorption velocities would imply that the  $v_{\text{LSR}} = +40$  km s $^{-1}$  gas lies at a line-of-sight distance that begins somewhere between the distance to HD 175876 and HD 175754. This places the near edge of the  $+40$  km s $^{-1}$  gas at between approximately 2.35 and 2.75 kpc from the Sun.

We observe the strong presence of moderately and highly ionized gas at a velocity that associates the absorption with the ejecta of the Supershell in the direction of HD 175754 and HD 177989. In particular, the lines of C iv and Si iv are extremely strong, and N v absorption is also probably detected. In these species, we are likely seeing transition-temperature gas associated with the ejecta of the Scutum Supershell (see § 5.5).

Integrated column densities for Al iii, Si iv, C iv, and N v toward HD 177989 reported by Sembach & Savage (1992) based on the apparent optical depth method are  $\log N(\text{Al iii}) = 13.38 \pm 0.02$ ,  $\log N(\text{Si iv}) = 13.87 \pm 0.17$ ,  $\log N(\text{C iv}) = 14.51 \pm 0.05$ , and  $\log N(\text{N v}) = 13.50 \pm 0.12$ . The column densities per unit velocity  $N(v)$  for these ions are seen in Figure 6 of Sembach & Savage (1992). The profile structure is such that the bulk of the absorption is associated with gas at approximately  $+30$  to  $+60$  km s $^{-1}$ , which implies that the major contribution to these column densities are occurring in gaseous absorption overlying the Scutum Supershell.

The full analysis of these UV absorption line observations is beyond the scope of this paper. In 1999 spring, the Space Telescope Imaging Spectrograph (STIS) was used to obtain very high resolution observations in the far-UV of

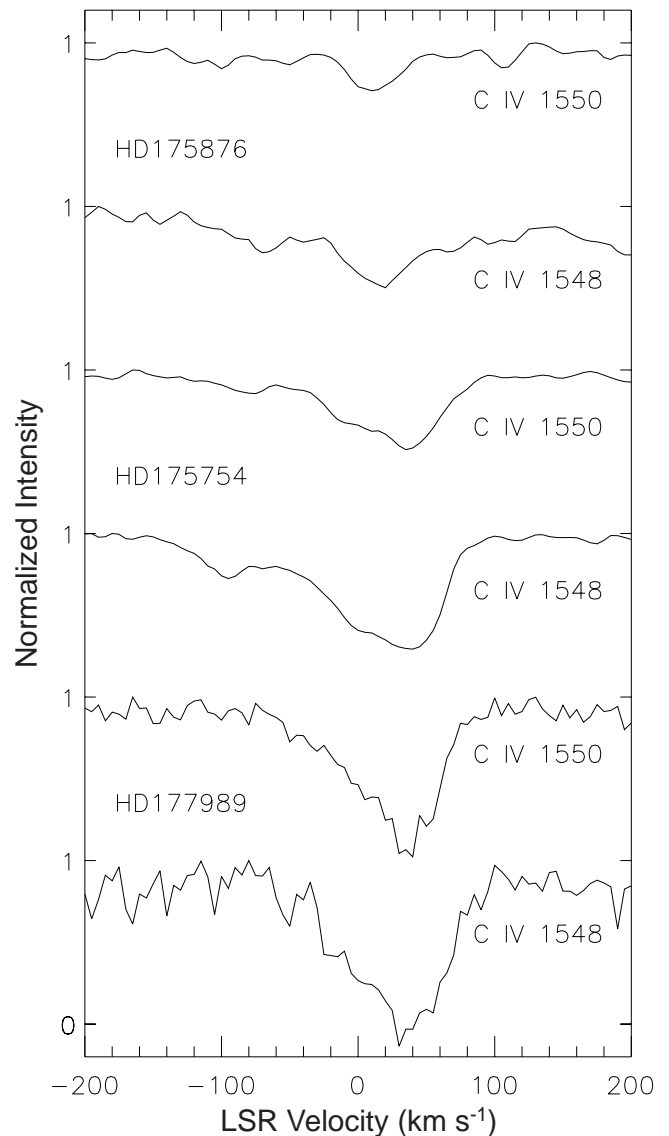


FIG. 11.—Continuum-normalized line profiles are illustrated for the C iv  $\lambda\lambda 1550.77$ ,  $1548.20$  absorption toward HD 175876, HD 175754, and HD 177989. HD 175876 exhibits only a relatively weak C iv component at  $v_{\text{LSR}} = +20$  km s $^{-1}$ , which is probably produced by absorption associated with gas in the Sagittarius spiral arm. The profiles for HD 175754 and HD 177989 show the  $+20$  km s $^{-1}$  absorption and in addition reveal strong contributions to C iv absorption by gas at  $v_{\text{LSR}} = +40$  km s $^{-1}$ . The  $+40$  km s $^{-1}$  absorption is likely mostly associated with gas in the high-latitude cloud lying above the Scutum Supershell. HD 175754 also exhibits C iv absorption produced in an intermediate negative-velocity cloud at  $-80$  km s $^{-1}$  (see Pottasch et al. 1980). Detailed component fits to the *IUE* observations and higher signal-to-noise ratio and higher resolution measurements to be obtained with STIS will be presented in future publications.

interstellar gas toward HD 177989 in order to study highly ionized gas associated with Galactic shells and supershells. The full analysis of the *IUE* data presented here will be included as part of that investigation. Based on the *IUE* data alone, it appears that the contribution to foreground gas is mostly confined to a lower velocity and relatively weak absorbing component as seen toward HD 175876 (see Figs. 10 and 11). The possible origin of the strong absorption by highly ionized gas associated with the Scutum Supershell is considered in § 5.5.

## 4. OBJECTS RELATED TO THE SCUTUM SUPERSHELL

Objects in the vicinity of the Scutum shell include H II regions, supernova remnants, massive stars, and molecular clouds. In particular we are interested in possible candidates for power sources. The high-latitude cloud of neutral material must have been propelled by a tremendous source of energy to achieve such a great distance from the Galactic plane. Previous studies of supershells (Heiles 1979, 1984; Koo et al. 1992; Maciejewski et al. 1996) have postulated multiple supernovae as primary candidates for supershell power sources. Other possibilities include the strong winds of stars in OB associations and H II regions (Koo et al. 1992). The proximity of the Scutum shell with these objects indicates a relationship. To clarify the presence of star-forming regions, we look for the presence of molecular clouds, almost sure indicators of star formation regions. This section presents the following data: O stars from the catalog of Garmany et al. (1982); H II regions from the catalog of Lockman (1989); and, finally, supernova remnants from the catalog of Green (1998).

Koo et al. (1992) note that their galactic worms GW 14.9–1.6 and GW 16.9–3.8 may be the walls of a supershell and remark that a candidate for an energy source is the Ser OB1 association, which is composed of nine O stars and 11 B stars, including one O4 and two O5 stars, between  $l = 15^\circ$  and  $19^\circ$  (Humphreys 1978). Eight of these O and B

stars lie below the plane of the Galaxy, between  $b = 0^\circ$  and  $-1.3^\circ$ . It seems likely that other stars in the region may also contribute energy in the form of winds. A list of all O stars was compiled from Garmany et al. (1982) and plotted on the H I emission map shown in Figure 12. Table 2 lists information from the Garmany catalog regarding O stars in the Scutum shell region. The O stars in the region are likely to be sources of ionizing radiation. Supernova remnants from Green (1998) are also displayed in Figure 12 with the O stars, and notable H II regions from the Lockman (1989) survey are included as well. The presence of hot, young stars in the Scutum shell region supports the idea that winds from these stars could be heating material in the Scutum shell. Distance uncertainties introduce a corresponding level of uncertainty with this claim.

The presence of three dense molecular clouds between  $l = 14^\circ$  and  $19^\circ$ , all at velocities corresponding to the Scutum shell, suggests that sites of active star formation do in fact coincide with the Scutum shell. Dame et al. (1986) see distinct molecular cloud structures in the region between  $l = 12^\circ$  and  $l = 25^\circ$ . Three of these clouds have velocities corresponding to the Scutum shell. These are labeled in Figure 12 according to their longitude and velocity. The notable clouds lie at  $l = 17^\circ$   $v = +44$  km s $^{-1}$ ,  $l = 18^\circ$   $v = +48$  km s $^{-1}$ , and  $l = 20^\circ$   $v = +42$  km s $^{-1}$ . Specifically interesting is the cloud at  $l = 20^\circ$  and  $v = +42$  km s $^{-1}$ . Not only is the radial velocity remarkably well matched to the

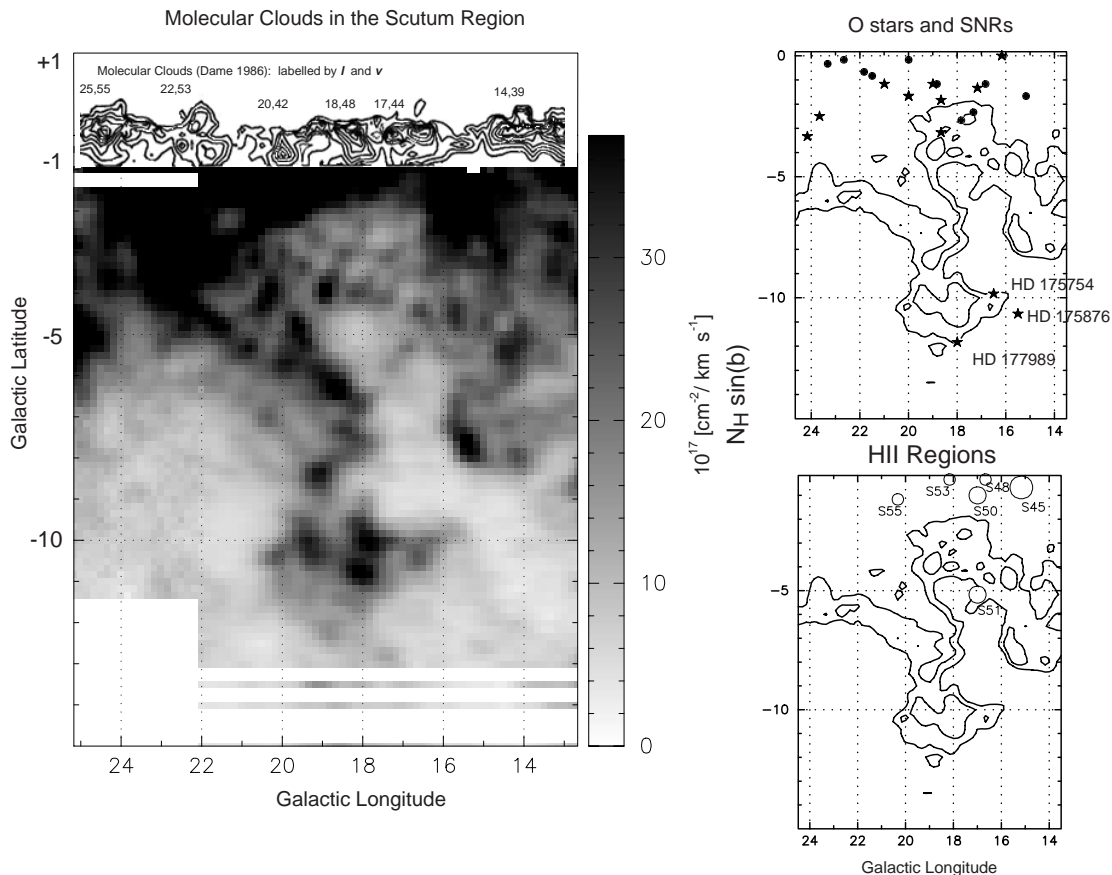


FIG. 12.—*Left*: Dame et al. (1986) CO survey. Here we see the presence of three molecular cloud complexes at the base of the Scutum shell. The three CO clouds between  $l = 16^\circ$  and  $20^\circ$  closely correspond to H II regions (*open circles in the lower right panel*). *Upper right*: Locations of O stars from the Garmany et al. (1982) catalog together with SNRs of Green (1998). Winds from young, hot stars can be connected to the energy source of the Scutum shell. The star symbols denote the O stars and the closed circles are the SNRs. The three stars studied in UV absorption are also marked. Two of these (HD 175754 and HD 175876) are O stars. The third (HD 177989) is a very distant B star.

Scutum shell's central velocity, but its bulblike morphology extends directly into the region of peak 1.5 keV X-ray emission.

The Lockman catalog of Galactic H II regions illustrates the Galactic spiral structure along the sight line toward the Scutum shell region. Figure 9 of Dame et al. (1986) displays structure traced by molecular clouds. Our Figure 1 is a reproduction of this structure traced by O stars, H II regions, and molecular clouds. 74 H II regions lie between  $l = 15^\circ$  and  $25^\circ$ . Table 1 lists relevant data on H II regions in the Scutum shell region. It is notable that 11 H II regions lie in a group associated with radial velocities between  $+40$  and  $+50$  km s $^{-1}$  and are therefore associated with the Scutum shell region. We can identify the amount of ionizing flux provided by these H II regions and compare that with the value necessary to produce the level of H $\alpha$  emission seen in the WHAM survey (§ 3.4).

Perhaps most importantly, supernova explosions are also possible sources of energy, with typical energies of  $\sim 10^{51}$  ergs. The Green (1998) catalog displays the existence of 10 supernova remnants in the region of the Scutum shell. Figure 12 shows a plot of the Green survey from  $l = 10^\circ$  to  $20^\circ$  and  $b = 1^\circ$  and  $-3^\circ$ . Without distance information, it is difficult to determine whether these lie within the region in question, but, because supernova have been considered primary energy candidates for supershells, we cannot ignore the possibility of their influence on the region. A complication arises when we consider that supernova remnants (SNRs) observed in radio wavelengths most likely lie within regions of ambient gas. If the Scutum shell has been evacuated, it may be unlikely that observed SNRs would be associated with the Scutum interior.

## 5. PHYSICAL CHARACTERISTICS OF THE SCUTUM SUPERSHELL

In this section we derive physical parameters of the Scutum Supershell based on the observed data. Each data set yields specific quantities, so each data set is treated individually.

### 5.1. Size, Mass, and Energy of the Scutum Supershell

In determining physical parameters, we consider two regions in the Scutum neighborhood, the supershell itself and the high-latitude cloud of neutral material at  $b = -11^\circ$ . We place the centroid of the Scutum Supershell at  $l = 17^\circ 5'$ ,  $b = -4^\circ 0'$ , at a velocity of  $+44$  km s $^{-1}$ , corresponding to a kinematic distance of 3.3 kpc using the Clemens (1985) rotation curve. At this longitude and distance from the sun, the distance to the center of the Galaxy is 5.44 kpc. The supershell subtends  $5^\circ$ , which, at 3.3 kpc, corresponds to a diameter of 290 pc. Since the shell walls are not clearly distinguishable we assume a shell thickness,  $\Delta R$ , of 20% of the total radius, or 29 pc. The volume of the spherical shell is then  $6.2 \times 10^6$  pc $^3$ . We estimate the mass by integrating the observed column density per unit velocity in one wall of the shell over the line of sight through the center of the shell. The profile demonstrating the strongest double peaks corresponds to  $l = 18^\circ$ ,  $b = -3^\circ 3'$  and is shown in Figure 4. We chose the H I profile with the double-peaked structure to calculate the column density because it has the strongest peak, providing an upper bound on mass calculations. We assume that the two peaks are at  $+36$  km s $^{-1}$  and  $+68$  km s $^{-1}$ , corresponding to the front and the back of the shell. The peak value for one wall is  $3.60 \times 10^{19}$  cm $^{-2}$  (km s $^{-1}$ ) $^{-1}$

with an FWHM of 10 km s $^{-1}$ . Thus the column density  $N_{\text{H}} = 3.6 \times 10^{20}$  cm $^{-2}$ . We then estimate a number density in the shell walls:

$$n_{\text{H}}(\text{cm}^{-3}) = \frac{N_{\text{H}}}{\Delta R} = 4.05. \quad (2)$$

The total mass in the shell walls is then

$$M(M_{\odot}) = 1.4 \frac{n_{\text{H}} m_{\text{H}} V}{M_{\odot}} = 8.68 \times 10^5, \quad (3)$$

where the 1.4 includes a correction for He.

While the double-peaked structure of the 21 cm emission line provides some evidence for an expanding shell, we note that not all sight lines through the shell demonstrate this double-peaked nature. Thus, we use Heiles' formulation for the energy of the shell, assuming that the shell is not rapidly expanding. An approximation of total energy (kinetic + thermal) required to create a shell that is expanding into a uniform medium, whose velocity has dropped to 8 km s $^{-1}$ , is given by Heiles (1979)

$$E(\text{ergs}) = 5.3 \times 10^{44} n_0^{1.12} R^{3.12} = 1.14 \times 10^{52}, \quad (4)$$

where  $n_0$  is the ambient density, calculated by assuming that all of the ambient mass has been swept into the shell walls. Here  $n_0 = 1.96$  cm $^{-3}$  and  $R = 145$  pc.

An approximate estimate of the age of the bubble can be calculated from an empirical formula derived by Tomisaka & Ikeuchi (1986), assuming constant energy input of one  $10^{51}$  ergs supernova every  $2 \times 10^5$  yr:

$$t(\text{Myr}) = \frac{(z_{\text{up}} - z_{\text{es}})^{2.3}}{16,000} [n(z_{\text{up}})]^{0.6}, \quad (5)$$

where  $z_{\text{es}}$  is the height of the energy source,  $z_{\text{up}}$  is the height of the top of the shell above the Galactic plane in parsecs, and  $n(z)$  is the gas density at a given height. We use  $z_{\text{es}} = 50$  pc, corresponding to the 1.5 keV X-ray-emitting gas at the base of the shell,  $z_{\text{up}} = 345$  pc, corresponding to the missing top of the shell at  $b = -6^\circ$ , and  $n(z) = n_0 = 1.96$  cm $^{-3}$ , as previously calculated. These values give us a rough estimate of  $4.5 \times 10^7$  yr for the age of the shell.

Turning our attention to the high-latitude cloud we calculate similar quantities. Figure 4 includes H I velocity profiles through the high-latitude cloud at  $b \sim -10^\circ$ . It is noteworthy that profiles through this cloud show peak emission between the two peaks revealed in spectra taken through the center of the shell, demonstrating that the cloud lies at a kinematic distance between the near and far walls of the shell. Assuming the cloud to be roughly spherical, we estimate its diameter to be 173 pc. The integrated velocity profile over 20 km s $^{-1}$  translates to a column density of  $3.0 \times 10^{20}$  cm $^{-2}$ , suggesting an average density of 0.56 cm $^{-3}$  in the cloud. Using equation (3), we estimate that the high-latitude cloud contains a mass  $M = 3.74 \times 10^4 M_{\odot}$ . Given a gravitational acceleration adopted from Ferrier (1998),

$$g(z, R)(\text{cm s}^{-2}) = 4.4 \times 10^{-9} \exp\left(-\frac{R - R_{\odot}}{4.9 \text{ kpc}}\right) \times \frac{z}{\sqrt{z^2 + 0.2^2}} + 1.7 \times 10^{-9} \frac{R_{\odot}^2 + 2.2^2}{R^2 + 2.2^2} \frac{z}{1 \text{ kpc}}, \quad (6)$$

and integrating to a height  $z$  of 630 pc, we find a potential energy of  $2.81 \times 10^{51}$  ergs, the energy of a few supernovae.

### 5.2. Dust Characteristics and $H_2$ Content of the High-Latitude Cloud

Measurements of infrared surface brightness can reveal some information about the nature of the high-latitude cloud. Studies of infrared excess emission done by Heiles, Reach, & Koo (1988) and Reach, Wall, & Odegard (1998) indicate that infrared emission above a baseline level may indicate the presence of molecular hydrogen in regions of high column density H I. We measure the infrared surface brightness from the *IRAS* 60 and 100  $\mu\text{m}$  maps within an appropriately sized rectangular region of the high-latitude cloud of H I seen in the NRAO survey. A baseline level was determined by measuring the surface brightness in neighboring regions at similar latitudes in an attempt to avoid complications due to the strong gradient with latitude in infrared emission.

An infrared surface brightness excess of  $6.23 \text{ MJy sr}^{-1}$  is found for the 100  $\mu\text{m}$  emission, and  $1.64 \text{ MJy sr}^{-1}$  for the 60  $\mu\text{m}$  emission. The ratio of infrared surface brightness excess to the H I column density associated with the cloud gives us information about the nature of the origins of this excess emission. The ratio of the average 100  $\mu\text{m}$  emission in our rectangular region to the average H I column density in the same region of the high-latitude cloud is

$$\frac{S(100)}{N_{\text{HI}}} [\text{MJy sr}^{-1}(10^{20} \text{ cm}^{-2})^{-1}] = 6.11. \quad (7)$$

We find clumpy regions in the high-latitude cloud with column densities as high as  $\sim 8 \times 10^{20} \text{ cm}^{-2}$ . Heiles et al. (1988) suggest that, in regions where H I column density are greater than  $\sim 2.4 \times 10^{20} \text{ cm}^{-2}$ , a departure of  $S(100)/N(\text{H I})$  from a value of  $1.3 \text{ MJy sr}^{-1}(10^{20} \text{ cm}^{-2})^{-1}$  may indicate the presence of molecular hydrogen. Reach et al. (1998) suggest that the column density of molecular hydrogen implied by an infrared excess can be expressed by the ratio

$$\frac{S(100)}{N(H_2)} [\text{MJy sr}^{-1}(10^{20} \text{ cm}^{-2})^{-1}] = 0.26 \pm 0.05, \quad (8)$$

thus implying that  $N(H_2)$  for the high-latitude cloud could be as large as  $2.4 \times 10^{21} \text{ cm}^{-2}$  in the dense portions of the cloud.

An alternate explanation for the IR excess is enhanced heating in the region of the high-latitude cloud. The close proximity of several luminous O stars including HD 175754 and HD 175876 (see § 3.5) makes this a viable possibility. Intense radiation emitted by the high-latitude O stars may be enough to heat the dust in the region, causing the observed infrared emission excess. It is interesting to note, however, that if the high-latitude young stars were in fact born at or near their high-latitude positions, then a dense region of molecular gas may be expected in the region. If the stars instead migrated to their current locations, the dust may simply be ambient material heated by the nearby stars.

Heiles et al. (1988) suggest that the ratio of 60  $\mu\text{m}$  surface brightness to 100  $\mu\text{m}$  surface brightness is an indication of grain size. They claim that a departure of this ratio from some normal value is an indication of grain processing by strong shocks. In their study of *IRAS* emission, a high value of  $S(60)/S(100)$  is  $\sim 0.29$ , which they attribute (according to Draine & Anderson 1985) to dust comprised mostly of

small grains, while a low, or “normal,” value is 0.21. We determine a ratio  $S(60)/S(100)$  of 0.26. This is a weak indication of dust destruction in the high-latitude material, indicative of shock processing. With such an interpretation, the *IRAS* measurements in this cloud suggest that some grain destruction has occurred.

### 5.3. X-Ray Luminosity

In this section, we attempt to distinguish the X-ray emission features from the regional soft X-ray background by quantifying the degree of enhancement. Both the absorption corrected and uncorrected X-ray maps were examined. To determine physical parameters, we used the maps that were corrected by the HB survey to ensure the largest coverage in Galactic latitude. In this manner we may examine the high-latitude features seen in the 0.25 keV emission maps and ensure consistency in comparison to maps of the 0.75 keV and 1.5 keV energy bands. The observed counts within several square regions of an emission map, away from X-ray enhancement features, are averaged to produce an average baseline emission. Average values of the X-ray enhancements are similarly calculated in appropriately sized square regions containing the enhancement features.

For example, the uncorrected 0.75 keV X-ray emission shows peaks at the base of the shell, within the blown-out top, and above the shell. The baseline was calculated from three  $2^{\circ}65 \times 2^{\circ}67$  square blocks away from the peak enhancements, covering  $21.2 \text{ deg}^2$ . The emission was averaged over all pixels in this region to produce an average baseline value of  $2.97 \times 10^{-4} \text{ counts s}^{-1} \text{ arcmin}^{-2}$ . An average enhancement of the feature in the blown-out top of the shell was calculated to be  $5.74 \times 10^{-4} \text{ counts s}^{-1} \text{ arcmin}^{-2}$  within a  $2^{\circ}65 \times 2^{\circ}67$  square box centered at  $l = 17^{\circ}67$ ,  $b = -14^{\circ}67$ . The average enhancement above the baseline is  $2.77 \times 10^{-4} \text{ counts s}^{-1} \text{ arcmin}^{-2}$ , an increase of 93%. This procedure was repeated for each of the corrected and uncorrected X-ray emission maps. Table 4 displays the specific parameters found for the baseline emission and enhancement regions for each image.

We convert our observed X-ray count rates to physical units of X-ray luminosity assuming spherical regions of hot gas, assuming that the emissivity is constant throughout the geometrical region. We find that the X-ray luminosity is related to the observed flux by

$$L_X(\text{ergs s}^{-1}) = \frac{8\pi}{3} d^2 F, \quad (9)$$

where  $d$  is the distance to the object and the flux  $F$  ( $\text{ergs cm}^{-2} \text{ s}^{-1}$ )  $= I\Omega R(T)$ , where  $I$  ( $\text{counts s}^{-1} \text{ arcmin}^{-2}$ ) is the instrumental intensity,  $R(T)$  ( $\text{ergs count}^{-1} \text{ cm}^{-2}$ ) is the instrumental conversion factor, and the angular size of the object is  $\Omega$  ( $\text{arcmin}^2$ ). Luminosities are calculated from the observed counts above the baseline for conspicuous X-ray emission features. With these counts and the observed angular size of the object known, we need only to calculate the conversion factors for count rates in each energy band.

It should be noted that all of our quoted X-ray luminosities correspond to the energy range 0.11–2.40 keV. We use the Raymond/Smith X-ray emission code and the *ROSAT* response matrix to produce a model count rate for the assumed temperatures,  $\log T = 7.0$  and  $\log T = 6.5$ . The XSPEC fitting software (Arnaud 1996) gives the corresponding flux for a given range of photon energies. The

TABLE 4  
UNCORRECTED X-RAY ENHANCEMENT PROPERTIES

X-RAY IMAGE	LOCATION <i>l/b</i> (deg)	UNCORRECTED X-RAY IMAGES ( $10^{-4}$ counts $s^{-1}$ arcmin $^{-2}$ )				ENHANCEMENT (%)	NOTES
		Total Counts	Average Foreground	Net Enhancement			
0.25 keV .....	17.67/–16.67	5.32	3.36	1.96	58	High latitude	
0.75 keV .....	18.00/–2.67	4.10	2.19	1.91	87	Within shell	
	16.67/–8.67	4.40	...	2.21	1.00	Shell top	
	17.67/–14.67	4.02	...	1.83	84	Above shell	
1.50 keV .....	18.67/–1.67	4.11	1.75	2.36	135	Shell base	
	17.00/–5.00	3.65	...	1.90	1.09	Within shell	

ratio of the total emitted flux from the entire model spectrum to the count rate of the specific observed energy band gives us the conversion factor  $R(T)$  to transform that band's count units into flux units. For example, our model emission for  $\log T = 7.0$  gives a flux of  $2.83 \times 10^{-9}$  ergs  $s^{-1}$   $cm^{-2}$  for the complete energy range accessible by *ROSAT*, 0.11–2.40 keV (assuming that all absorption has been properly removed). The model-predicted count rate for the 0.75 keV band (the 0.44–1.21 keV range) is 8.96 counts  $s^{-1}$ . Thus the conversion factor for this energy band is  $R(T)(\text{ergs count}^{-1} \text{ cm}^{-2}) = 3.16 \times 10^{-10}$ . This conversion factor can be applied to the observed 0.75 keV counts above baseline for each enhancement feature. The mid-latitude feature displays  $3.26 \times 10^{-4}$  counts  $s^{-1}$  arcmin $^{-2}$  above baseline and an angular size of 39,800 arcmin $^2$  and therefore corresponds to a total X-ray flux of  $4.10 \times 10^{-9}$  ergs  $s^{-1}$   $cm^{-2}$ . This flux, at a distance of 3300 pc, gives an X-ray luminosity of  $3.56 \times 10^{36}$  ergs  $s^{-1}$ . This process is repeated for each of the X-ray enhancement features in the *ROSAT* maps.

Table 5 displays the model data for assumed parameters and the corresponding conversion factors. For example, the 1.5 keV emission map corresponds to *ROSAT* energy bands R6 and R7, or a photon energy range of 0.73–2.04 keV. We compute a model-predicted count rate of 11.38 counts  $s^{-1}$  for this band at a temperature of  $\log T = 7.0$ . For this temperature, the total flux for the entire *ROSAT* energy range is  $2.83 \times 10^{-9}$  ergs  $s^{-1}$   $cm^{-2}$ . Thus, for the 1.5 keV emission features, we calculate a conversion factor  $R(\log T = 7.0)(\text{ergs count}^{-1} \text{ cm}^{-2}) = 2.49 \times 10^{-10}$ . We observe  $3.57 \times 10^{-4}$  counts  $s^{-1}$  arcmin $^{-2}$  above baseline for the feature at  $b = -8^\circ$ , in an angular size of  $2.55 \times 10^4$  arcmin $^2$ , yielding a total flux of  $2.27 \times 10^{-9}$  ergs  $s^{-1}$   $cm^{-2}$ ,

corresponding to a luminosity of  $1.97 \times 10^{36}$  ergs  $s^{-1}$ . Table 6 displays the calculated X-ray luminosity of the Scutum shell region based on each of the primary enhancement features.

Our method demonstrates the difficulty in quantifying the X-ray emission. Without spectral information, we are forced to make a best guess for the temperature of the emitting gas. Coupled with the difficult determination of foreground absorbing material, we are restricted by large uncertainties in determining true X-ray luminosities. Our estimates do provide an order-of-magnitude value. We calculate an X-ray luminosity of  $\sim 6\text{--}8 \times 10^{36}$  ergs  $s^{-1}$  for the Scutum shell interior,  $\sim 1\text{--}4 \times 10^{36}$  ergs  $s^{-1}$  for the blown-out top of the shell, and  $\sim 0.3\text{--}17 \times 10^{36}$  ergs  $s^{-1}$  for the high-latitude feature.

#### 5.4. Warm Ionized Medium Emission Measure

To estimate physical characteristics implied by the H $\alpha$  emission, we must remove the effects of foreground attenuation and calculate an emission measure. We restrict ourselves to the  $+40$  km  $s^{-1}$  velocity emission map to examine gas at the kinematic distance of the Scutum shell. Even in this map, the H $\alpha$  morphology displays distinct structures that we can identify with H II regions not associated with the Scutum shell region. The H II regions S45 and S55 dominate the H $\alpha$  emission maps. A number of H II regions lie in the Scutum shell latitude, longitude, and velocity region, but the H $\alpha$  is by far brightest for S45, which lies at  $+20$  km  $s^{-1}$ . The close proximity of S45 imposes some confusion upon the more distant emission. Emission spectra clearly show multiple component structure. To be certain that we are determining physical parameters for only the

TABLE 5  
MODEL PARAMETERS FOR THE *ROSAT* INSTRUMENT

Emission Map	<i>ROSAT</i> Energy Band	Energy Range (keV)	Model Counts (counts $s^{-1}$ )	Model Flux (ergs $s^{-1}$ $cm^{-2}$ )	Conversion Factor $R(T)$ (ergs $cm^{-2}$ count $^{-1}$ )
$\log T = 6.5$					
0.25 keV .....	R1–R2	0.11–0.28	21.86	...	$1.36 \times 10^{-10}$
0.75 keV .....	R4–R5	0.44–1.21	11.59	...	$2.56 \times 10^{-10}$
1.5 keV .....	R6–R7	0.73–2.04	3.89	...	$7.63 \times 10^{-10}$
All .....	R1–R8	0.11–2.40	47.33	$2.97 \times 10^{-9}$	$6.28 \times 10^{-11}$
$\log T = 7.0$					
0.25 keV .....	R1–R2	0.11–0.28	11.34	...	$2.43 \times 10^{-10}$
0.75 keV .....	R4–R5	0.44–1.21	8.96	...	$3.16 \times 10^{-10}$
1.5 keV .....	R6–R7	0.73–2.04	11.38	...	$2.49 \times 10^{-10}$
All .....	R1–R8	0.11–2.40	37.53	$2.83 \times 10^{-9}$	$7.54 \times 10^{-11}$

TABLE 6  
OBSERVED X-RAY PROPERTIES OF THE SCUTUM SHELL

Observed X-Ray Feature	Area ( $10^3$ arcmin $^2$ )	Average $\log N_{\text{H}}$ ( $\text{cm}^{-2}$ )	Observed $L_{\text{X}}$ ( $\text{ergs s}^{-1}$ )
$b = -2^\circ$ , 0.75 keV .....	6.37	21.37	$6.65 \times 10^{36}$
$b = -2^\circ$ , 1.5 keV .....	6.37	21.37	$8.27 \times 10^{36}$
$b = -8^\circ$ , 0.75 keV .....	39.8	21.17	$3.56 \times 10^{36}$
$b = -8^\circ$ , 1.5 keV .....	25.5	21.17	$1.97 \times 10^{36}$
$b = -13^\circ$ , 0.75 keV .....	25.5	20.94	$1.53 \times 10^{36}$
$b = -13^\circ$ , 1.5 keV .....	14.3	20.94	$3.56 \times 10^{35}$
$b = -15^\circ$ , 0.25 keV .....	25.5	20.94	$1.73 \times 10^{37}$

Scutum shell region, we ignore the S45 region and focus on S55, which can be more clearly associated with the Scutum shell. We calculate the emission measure (EM) within the S55 region and associate it with the interior of the Scutum shell.  $\text{H}\alpha$  intensity in the S55 H II region is determined by integrating over a Gaussian fit to the component centered at  $+40 \text{ km s}^{-1}$ . For the high-latitude cloud of  $\text{H}\alpha$  emission, the intensity is determined by integrating over  $+40 \text{ km s}^{-1}$  Gaussian components in four WHAM beams, covering a  $2^\circ \times 2^\circ$  region of the cloud near  $b = -10^\circ$ , and averaging the result.

To correct for foreground absorption, we attempt to deredden the observed  $\text{H}\alpha$  emission. While the calculation involves large uncertainties, we cannot ignore the effects of foreground extinction. We have selected a  $1^\circ \times 1^\circ$  square region from HB centered on S55, where we find an average H I column density of  $1.21 \times 10^{22} \text{ cm}^{-2}$ . Using the conversion ratio of Diplas & Savage (1994), this column represents an average  $E(B-V) = 2.45$ , corresponding to an optical depth at  $\text{H}\alpha$ ,  $\tau = 6.72$ , using the extinction curve of Cardelli et al. (1989). The integrated  $\text{H}\alpha$  emission in this  $1^\circ$  region is 87.5 Rayleighs (1 R =  $10^6/4\pi$  photons  $\text{cm}^{-2} \text{ s}^{-1} \text{ sr}^{-1}$ , or  $2.4 \times 10^7 \text{ ergs cm}^{-2} \text{ s}^{-1} \text{ sr}^{-1}$ ). Thus the absorption corrected  $\text{H}\alpha$  emission is 72,500 R, a correction factor of 830. Physical parameters may be derived from the absorption corrected  $\text{H}\alpha$  intensity. We convert intensity to emission measure according to Haffner, Reynolds, & Tufte (1998):

$$\text{EM}(\text{cm}^{-6} \text{ pc}) = 2.75 T_4^{0.9} \langle I_{\text{H}\alpha} \rangle, \text{ corrected}, \quad (10)$$

where  $T_4$  represents the temperature of the emitting gas in units of  $10^4 \text{ K}$  and  $I$  is in Rayleighs. With a typical  $T_4 = 0.8$  for the warm ionized medium (Reynolds 1985), an  $\text{H}\alpha$  intensity of 1 R corresponds to an EM of  $2.25 \text{ cm}^{-6} \text{ pc}$ . With an absorption corrected integrated  $\text{H}\alpha$  intensity of  $7.25 \times 10^4 \text{ R}$  in the S55 region, we find  $\text{EM} = 1.63 \times 10^5 \text{ cm}^{-6} \text{ pc}$ . This should be compared to an uncorrected emission measure EM of  $1.97 \times 10^2 \text{ cm}^{-6} \text{ pc}$ . Such extremely large values may not be physically reasonable.

It is important to note the uncertainty imposed upon this value by our assumption that all of the observed H I is foreground. For example, if we were to instead assume that 80% of the observed H I were foreground, we obtain an extinction  $E(B-V)$  of 1.96, an optical depth  $\tau = 5.38$ , and an emission measure EM of  $4.27 \times 10^4 \text{ cm}^{-6} \text{ pc}$ , a decrease of 75%. The longitude of the Scutum shell lies in a sight line that looks tangentially through a spiral arm; thus we might expect that a substantial amount of H I lies on the far side of the Scutum region. Uncertainties regarding H I column density at low latitudes make derived physical parameters highly questionable. We have also ignored the effects of  $\text{H}\alpha$  scattering off of foreground dust into the beam of WHAM.

Thus, we are restricted to more qualitative discussion of phenomena near the plane. More detailed and accurate results could be obtained with direct measurements of foreground absorption toward bright stars in the Scutum shell region. A large number of O and B stars reside in the area; thus future absorption studies may certainly clarify the matter, as would future emission studies of  $\text{H}\beta$ . At the high latitudes, where intervening absorption is significantly smaller, such corrections do not significantly alter the measurements of EM. For example, at  $b = -20^\circ$ , the emission correction for 80% of the total  $N_{\text{H}}$  being foreground material is at most 5%.

The high-latitude  $\text{H}\alpha$  emission, at  $b = -10^\circ$ , indicates a two-component structure. Spectral fitting indicates that the  $+40 \text{ km s}^{-1}$  component dominates, being about a factor of 2 stronger than the  $+20 \text{ km s}^{-1}$  component. Averaging over four  $1^\circ$  beams centered on the high-latitude cloud of  $\text{H}\alpha$  emission gives an average integrated intensity of 6.80 R. Here we measure the average H I column density to be  $1.20 \times 10^{21} \text{ cm}^{-2}$ , corresponding to an extinction  $E(B-V) = 0.24$  and an  $\text{H}\alpha$  optical depth of 0.67. The absorption-corrected  $\text{H}\alpha$  intensity is therefore 16.3 R and the emission measure is  $29.9 \text{ cm}^{-6} \text{ pc}$ . This  $2^\circ$  region corresponds to a diameter of 115 pc. Assuming a uniform density, we estimate  $\langle n_e \rangle = 2.60 \times 10^{-1} \text{ cm}^{-3}$  at  $b = -10^\circ$ .

These parameters give some rough estimates on the physical conditions at high latitudes above the Scutum shell region. Observations of features near the plane are limited by the uncertainties imposed by the broad line width of the  $\text{H}\alpha$  emission, the geometrical distribution of material, and the determination of the true amount of extinction toward the  $\text{H}\alpha$  emission. It is clear, however, from the velocity profiles of the  $\text{H}\alpha$  emission that ionized material from nearby H II regions influences the Scutum shell region. The CO radial velocities for S48 and S53 place these two H II regions at the kinematic distance of the Scutum shell. S55 is the brightest  $\text{H}\alpha$ -emitting region in the  $\text{H}\alpha$  emission maps, and, although it has no associated CO detection, the WHAM data places its peak velocity at  $+40 \text{ km s}^{-1}$ , also within the Scutum shell region. The lack of a CO measurement by Lockman (1989) suggests that the S55 H II region may not be associated with star formation but may instead be a result of SNRs in the region. It is likely, in any case, that the S48, S53, and S55 H II regions inject a substantial amount of energy into the Scutum shell.

Regarding the vertical column of  $\text{H}\alpha$  emission between  $l = 18^\circ$  and  $19^\circ$ , the  $+40 \text{ km s}^{-1}$  map displays a column of  $\text{H}\alpha$  analogous to the H I column, suggesting a correlation between the neutral and ionized material. Gaussian fits to the  $\text{H}\alpha$  spectra suggest a double-peaked structure to this

high-latitude emission. One peak is centered at  $+20 \text{ km s}^{-1}$ , associated with the intense emission from the S45 H II region. The second peak is centered at  $+40 \text{ km s}^{-1}$ , associated with the S55 region. The two profiles blend with increasing latitude, forming a broad peak at  $+30 \text{ km s}^{-1}$ . The existence of an emission profile centered at  $+40 \text{ km s}^{-1}$  that extends to  $b = -10^\circ$  indicates the presence of ionized material that seems to originate in the S55 H II region and rise to large distances above the plane.

### 5.5. Highly Ionized Gas Overlying the Scutum Supershell

Much of the Si IV, C IV, and N V absorption toward HD 177989 occurs at a velocity that associates the absorption with the Scutum Supershell ejecta at a distance of  $\sim 700 \text{ pc}$  away from the Galactic plane (see § 3.5). In order to understand the spectroscopic signature the Scutum Supershell has imposed upon these observations, it is valuable to relate the high-ionization absorption toward HD 177989 to the absorption for other sight lines through Milky Way disk and halo gas. The most extensive recent discussions of the properties and origins of highly ionized gas in the Milky Way disk and halo are found in Sembach, Savage, & Tripp (1997) and Savage, Sembach, & Lu (1997). Sembach et al. (1997) have studied how the properties of highly ionized gas in Galactic Radio Loops I and IV compare to those for other directions. Savage et al. (1997) present the results of an *IUE* and *Hubble Space Telescope* (*HST*) study of highly ionized gas along Galactic and extragalactic sight lines. Both papers include results for HD 177989, which permits an assessment of how the absorption along this sight line compares to that in other Galactic directions.

The behavior of the high ion absorption in the lines of Si IV, C IV, and N V toward HD 177989 is similar to the behavior of these same absorption lines toward HD 119608, which lies  $4.1 \text{ kpc}$  in the direction  $l = 320^\circ.4$  and  $b = +43^\circ.1$ . The path to HD 119608 passes through the center of Galactic Radio Loop IV, which lies inside the boundaries of Radio Loop I. These radio loops trace local Galactic supershells that appear to be the remnants of a series of explosions in the Sco-Cen cluster (see discussion in Sembach et al. 1997). The high-ionization absorption toward HD 119608 and HD 177989 appear to be unusual in several ways. (1) In plots of  $N(\text{C IV}) \sin |b|$  versus  $|z|$  for a large number of objects, both HD 177989 and HD 119608 exhibit excess, of factors of 2.5 and 3.2, respectively, compared to the Galactic average (see Fig. 4 in Savage et al. 1997). A similar excess is found for the direction to 3C 273, which lies in a direction passing near the edge of Radio Loop IV. (2) The high ion ratios for HD 177989 and HD 119608 are unusual compared to other lines of sight; the values of  $N(\text{C IV})/N(\text{N V})$  toward HD 177989 and 119608 are  $10.2 \pm 2.7$  and  $10.7 \pm 2.1$ . These are the largest two values of this ratio measured for the entire set of disk and halo stars and extragalactic objects surveyed with the *IUE* and *HST* by Savage et al. (1997), who report an average ratio and dispersion  $\langle N(\text{C IV})/N(\text{N V}) \rangle = 4.6 \pm 2.4$ . While there is an excess in the C IV column density toward HD 177989 and 119608, the excess evidently is not reflected in the column density of N V. A similar factor of  $\sim 2$  excess is found for  $N(\text{Si IV})/N(\text{N V})$  for both sight lines, while  $N(\text{C IV})/N(\text{Si IV})$  is normal toward HD 177989 and 2 times larger than normal toward HD 119608.

In their study of highly ionized gas absorption toward Radio Loops I and IV, Sembach et al. (1997) have reviewed

the many theories advanced to explain the origin of the highly ionized gas in the ISM. The theories involving cooling fountain gas (Benjamin & Shapiro 2000), conductive interfaces (Borkowski, Balbus, & Fristro 1990), and hot gas in supernova bubbles (Slavin & Cox 1992) all predict values of  $N(\text{C IV})/N(\text{N V})$  substantially smaller than that observed toward HD 177989 and 119608. The theory that most closely matches the observations is the turbulent mixing layer model of Slavin, Shull, & Begelman (1993), in which hot gas ( $10^6 \text{ K}$ ) and cooler ( $10^2\text{--}10^4 \text{ K}$ ) gas mix in the presence of shear flows (Begelman & Fabian 1990) to produce intermediate-temperature gas containing transition-temperature ion states, including Si IV, C IV, N V and O VI. The region of the Scutum Supershell along the line of sight to HD 177989 and also Radio Loops I and IV may represent regions of shear flow and substantial turbulent mixing of warm and hot gas. For both sight lines there is evidence for hot gas (X-ray emission) and for warm neutral and warm ionized gas. The outflow associated with the energetic events occurring in each region may be the source of the shear flow. When higher quality *HST* STIS data for the sight line to HD 177989 become available, it will be interesting to study the observed conditions along the sight line to HD 177989 carefully and to make detailed comparisons with the predictions of the turbulent mixing layer model.

## 6. COMPARISON WITH OTHER SUPERSHELLS

To compare the Scutum shell with another well-known X-ray enhancement feature, we turn to the Orion-Eridanus supershell. The Eridanus shell lies  $\sim 400 \text{ pc}$  away and has a diameter of  $\sim 120 \text{ pc}$ . It spans  $35^\circ$  in Galactic latitude and  $20^\circ$  in Galactic longitude, centered at  $l = 200^\circ$ ,  $b = -32^\circ$ . It is notable that the Eridanus region lies in a direction away from the center of the Galaxy, at a latitude far from the plane, greatly reducing absorption effects due to intervening material, and the region has been studied extensively (e.g., Reynolds & Ogden 1979; Burrows et al. 1993; Snowden et al. 1995; Brown, Hartman, & Burton 1995). Burrows et al. (1993) use the *HEAO 1 A-2* LED experiment to determine X-ray properties of the Eridanus region. They identify two prominent enhancements in the 0.25 and 0.75 keV bands and calculate observed X-ray luminosities for both features. Snowden et al. (1995) use the *ROSAT* instrument to observe the region and identify the 0.25 keV feature as emission from more distant halo gas, stating that the 0.75 keV emission enhancement is the only feature associated with the Eridanus region. They also observe that the Eridanus region is not seen in the 1.5 keV *ROSAT* band. We therefore focus on the 0.75 keV feature of the Eridanus region.

Burrows et al. (1993) calculate a X-ray luminosity for the 0.75 keV feature by integrating emission over the 0.1–1.0 keV X-ray energy region and find  $L_X = 6.7 \times 10^{34} \text{ ergs s}^{-1}$ . This figure is based on a single-temperature Raymond/Smith model spectral fit for X-rays from a shell at a distance of 130 pc. The spectral fits of Burrows et al. (1993) suggest  $\log T = 6.3$  for the Eridanus X-ray 0.75 keV enhancement. They suggest that the X-rays may extend across an elongated bubble, reaching a distance of  $\sim 460 \text{ pc}$ . If the X-rays are actually being emitted from 400 pc, they suggest a luminosity of  $6.3 \times 10^{35} \text{ ergs s}^{-1}$  as more appropriate. Applying our methods, from § 3.3, to the Eridanus region, we estimate the prominent 0.75 keV enhancement region to occupy  $7.5 \times 10^5 \text{ arcmin}^2$ , with emission levels  $\sim 1.50 \times 10^{-4}$

counts  $\text{s}^{-1} \text{arcmin}^{-2}$  above baseline levels. Assuming that foreground absorption is minimal at these latitudes, we calculate a total flux of  $2.9 \times 10^{-8} \text{ergs s}^{-1} \text{cm}^{-2}$ , corresponding to a luminosity of  $3.88 \times 10^{34} \text{ergs s}^{-1}$  at a distance of 130 pc and  $3.70 \times 10^{35} \text{ergs s}^{-1}$  at a distance of 400 pc. This suggests that our methods, while incorporating large uncertainties, can give us a good estimate of X-ray luminosity based upon a reasonably assumed X-ray spectrum.

Burrows et al. (1993) suggest that the Eridanus X-ray enhancement is produced by the nearby superbubble, energized by the combined effects of stellar winds and supernova explosions from the Ori OB1 association. This view is supported by Reynolds & Ogden (1979), who observe H $\alpha$  filaments that could be explained by ionizing flux from Ori OB1. Brown et al. (1995) also corroborate that the energy required for the Eridanus bubble is the mechanical luminosity from stellar winds and supernovae in Orion OB1. The lack of 1.5 keV X-ray emission and the much lower value of X-ray luminosity suggest that the Eridanus region lacks the hotter gas observed in the Scutum shell. The phenomena producing the Scutum shell must impart a vast quantity of energy to the ISM in that region.

We may also compare our results to those of Chu et al. (1995), who calculate the X-ray luminosities of superbubbles in the Large Magellanic Cloud (LMC). They demonstrate four candidates as X-ray-dim superbubbles, having luminosities in the range  $2\text{--}10 \times 10^{34} \text{ergs s}^{-1}$ , and determine parameters for the LMC shells. By comparison, Chu et al. (1993) present studies of X-ray-bright supershells, with luminosities in the range  $1\text{--}350 \times 10^{35} \text{ergs s}^{-1}$ . Table 7 summarizes the observed physical parameters of the LMC shells studied by Chu et al. (1993), as well as those for the Eridanus shell. Table 6 displays similar parameters for the Scutum shell. Comparing the X-ray luminosity of the Scutum shell to those of the LMC, it appears that the Scutum shell would qualify as a typical X-ray bright shell. It is notable that LMC shells are viewed from above. A similar

perspective on the Scutum shell would superimpose the low-, mid-, and high-latitude features. This superposition would increase the observed X-ray luminosity to  $\sim 8.0 \times 10^{36} \text{ergs s}^{-1}$  (as calculated from the sum of the 0.75 keV luminosity values). This firmly places the Scutum shell within the X-ray-bright category of Chu et al.

Chu et al. suggest that the X-ray luminosity within supershells arises as a result of hidden supernova remnants (SNRs) within the shell. The SNRs deliver their energy to the ISM by driving the surrounding superbubbles rather than directly heating the ISM. An expanding SNR within a shell generates little excess X-ray emission because of the low densities ( $\sim 10^{-3} \text{cm}^{-3}$ ). X-ray intensities grow by orders of magnitude when the SNR encounters the denser edges of the shell (Chu et al. 1993, 1995). The X-ray emission from the Scutum shell does display some evidence for morphology associated with old SNRs. The limb brightening seen in the 0.75 and 1.5 keV emission is an example. A correlation between the 1.5 keV X-ray emission and the H $\alpha$  emission suggests a connection between a heavily active region near  $l = 20^\circ$ ,  $b = -1^\circ$  and the Scutum shell. Other objects in the region also contribute energy to the region, including supernova remnants. These objects are discussed in § 4. With the observed data suggesting an approximate value of the X-ray luminosity, it seems clear that the Scutum shell falls into the category of strong X-ray sources.

## 7. CONCLUSIONS

Table 8 summarizes the physical characteristics of the Scutum Supershell as derived in § 5.

1. We have examined data of the H I 21 cm radio emission and detected the presence of the Scutum Supershell centered at Galactic longitude  $l = 17^\circ 5'$ , latitude  $b = -4^\circ 0'$ , and LSR velocity  $+44 \text{km s}^{-1}$ . This velocity corresponds to a kinematic distance of  $\sim 3.3 \text{kpc}$ . At this distance, and subtending  $\sim 5^\circ$ , the shell has a diameter of 290 pc and

TABLE 7  
OBSERVED PROPERTIES OF X-RAY-EMITTING SHELLS

Object Name	Area (arcmin <sup>2</sup> )	Average log $N_{\text{H}}$ (cm <sup>-2</sup> )	Observed $L_{\text{X}}$ (ergs s <sup>-1</sup> )
X-Ray-dim LMC Shells <sup>a</sup>			
DEM 31 .....	48	20.0	$10\text{--}3 \times 10^{34}$
DEM 105 .....	60	21.24	$19\text{--}4.5 \times 10^{34}$
DEM 106 .....	16.5	21.24	$9\text{--}2 \times 10^{34}$
DEM 137 .....	178	20.93	$14\text{--}4 \times 10^{34}$
X-Ray-bright Shells in N44 <sup>b</sup>			
Shell 1 .....	16.6	22.0–21.8	$350\text{--}29 \times 10^{35}$
Shell 2 .....	18.8	21.2–20.4	$1.1\text{--}0.58 \times 10^{35}$
Shell 3 .....	10.4	21.2–20.5	$1.5\text{--}1.1 \times 10^{35}$
South Bar .....	17.8	21.9–20.5	$184\text{--}0.96 \times 10^{35}$
North Diffuse .....	55.5	20.5–19.5	$1.2\text{--}0.78 \times 10^{35}$
The Eridanus Supershell <sup>c</sup>			
EXE1: Eridion Bubble .....	$2.2 \times 10^6$	20.0	$6.7 \times 10^{34}$

<sup>a</sup> Converted to luminosity by the energy conversion factor (ECF) curves of the ROSAT Mission Description. From Chu et al. 1995, calculated using ROSAT bands R4–R7 or the 0.44–2.04 keV energy range.

<sup>b</sup> From Chu et al. 1993, calculated using ROSAT bands R4–R7 or the 0.44–2.04 keV energy range.

<sup>c</sup> From Burrows et al. 1993, calculated from spectral fits to HEAO 1 M-band or 0.4–0.9 keV energy range data.

TABLE 8  
PROPERTIES OF THE SCUTUM SHELL AND THE  
HIGH-LATITUDE CLOUD

Parameter	Value
Scutum Supershell	
Kinematic distance (pc) .....	3300
Diameter (pc) .....	290
Volume (pc <sup>3</sup> ) .....	$6.2 \times 10^6$
H I column (cm <sup>-2</sup> ) .....	$3.6 \times 10^{20}$
H I density (cm <sup>-3</sup> ) .....	4.05
Mass ( $M_{\odot}$ ) .....	$6.20 \times 10^5$
Total energy (ergs) .....	$1.14 \times 10^{52}$
$L_{X\text{-ray}}$ (ergs s <sup>-1</sup> ) .....	$\sim 5 \times 10^{36}$
High-Latitude Cloud	
Height $z$ (pc) .....	630
Diameter (pc) .....	173
Volume (pc <sup>3</sup> ) .....	$2.71 \times 10^6$
H I column (cm <sup>-2</sup> ) .....	$3.1 \times 10^{20}$
H I density (cm <sup>-3</sup> ) .....	0.56
Mass ( $M_{\odot}$ ) .....	$3.74 \times 10^4$
Potential energy (ergs) .....	$2.81 \times 10^{51}$
$EM_{\text{WIM}}$ (cm <sup>-6</sup> pc) .....	30
$S(100)/N_{\text{HI}}$ .....	6.11
$S(60)/S(100)$ .....	0.26

extends to about 400 pc from the Galactic plane. The top of the shell appears to have been blown away, leaving a rising column of neutral hydrogen at  $l = 18^{\circ}$ , culminating in a large high-latitude cloud. This cloud subtends  $\sim 5^{\circ}$ , with its upper edge at  $-12^{\circ}$  latitude, placing it at a vertical distance of 670 pc from the Galactic plane, along the sight line toward the star HD 177989. The observed properties of the Scutum Supershell and its high-latitude cloud are given in Table 8.

2. We have presented data from the *ROSAT* all-sky X-ray survey. These data show strong relationships to the 21 cm data and strengthen the morphological features of the Scutum shell. The X-rays reveal the existence of hot gas extending from the plane of the Galaxy, through the shell, and into the high-latitude region beyond  $b = -12^{\circ}$ . X-ray luminosity is estimated to be  $\sim 10^{36}$  ergs s<sup>-1</sup> for each of the three major emission features, one at low latitudes within the shell, one at mid latitudes in the blown-out region, and one at high latitudes. The values of X-ray luminosity are consistent with X-ray bright supershells in the LMC, as described by Chu et al. The Scutum shell is significantly more luminous than the Eridanus X-ray enhancement.

3. We have presented data from the WHAM all-sky H $\alpha$  survey. The H $\alpha$  data demonstrate the presence of ionized hydrogen within the bounding velocities of the Scutum shell

walls and also correlate with the rising column of neutral hydrogen. The X-ray and H $\alpha$  emission suggest a power source heating the gas in the region of the shell and forcing it upward to high latitudes. These data, along with the apparent deficiency in H I emission at  $b = -8^{\circ}$ , then reinforce the picture of a blown-out supershell, with its contents being thrust out of the plane of the Galaxy and into the halo. Estimates of emission measure are restricted to high latitudes, where foreground absorption is minimized. In these regions, we find  $EM \sim 30$  cm<sup>-6</sup> pc and  $\langle n_e \rangle = 0.26$  cm<sup>-3</sup>.

4. Ultraviolet high-dispersion spectra of HD 177989 ( $l = 17^{\circ}89$ ,  $b = -11^{\circ}88$ ) and HD 175754 ( $l = 16^{\circ}40$ ,  $b = -9^{\circ}92$ ) obtained with the *IUE* reveal the presence of very strong absorption by highly ionized gas, including Si IV, C IV, and N V, at a velocity that associates the absorption with the ejecta of the Scutum Supershell. In the case of HD 177989, the high ion column density ratios suggest an origin in a turbulent mixing layer where hot and cool gases mix in the presence of shear flows. The energetic events that have resulted in the expulsion of the high-latitude cloud from the disk may be the source of the shear flow creating the mixing.

5. The Scutum region includes many hot stars, supernova remnants, and H II regions that stand out as primary power sources. The combination of these objects may produce an amount of energy that could power the blowout of a supershell. The objects seem well positioned to power a continuing evolution of the feature and account for the large amount of gas at such a great distance from the Galactic plane.

6. In the Scutum shell region, we see a multitude of powerful energy sources ionizing a great deal of material and ejecting it from the confines of a Galactic shell. This observational evidence demonstrates a mechanism by which hot material can be ejected from the plane of the Galaxy and injected into the halo. Future studies with the STIS instrument and the *FUSE* satellite should clarify the abundances of highly ionized species and tell us something about the processes of dust destruction along the HD 177989 sight line.

We thank J. Lockman and E. Murphy for the use of the NRAO H I data set. We acknowledge the use of NASA's SkyView facility<sup>4</sup> at NASA Goddard Space Flight Center and the SIMBAD database, operated at CDS, Strasbourg, France.

<sup>4</sup> NASA's SkyView facility is available on the World Wide Web at <http://skyview.gsfc.nasa.gov>.

## APPENDIX

### CALCULATION OF X-RAY LUMINOSITIES

Pointed X-ray observations made with *ROSAT* are usually processed using data reduction software such as XSPEC (Arnaud 1996). This allows one to fold an assumed spectral shape (which in this case is a complicated line and continuum spectrum from a single-temperature thermal gas) through an energy-dependent absorbing foreground and the detector-telescope effective area and energy response function. In this Appendix, we include all the information necessary to convert

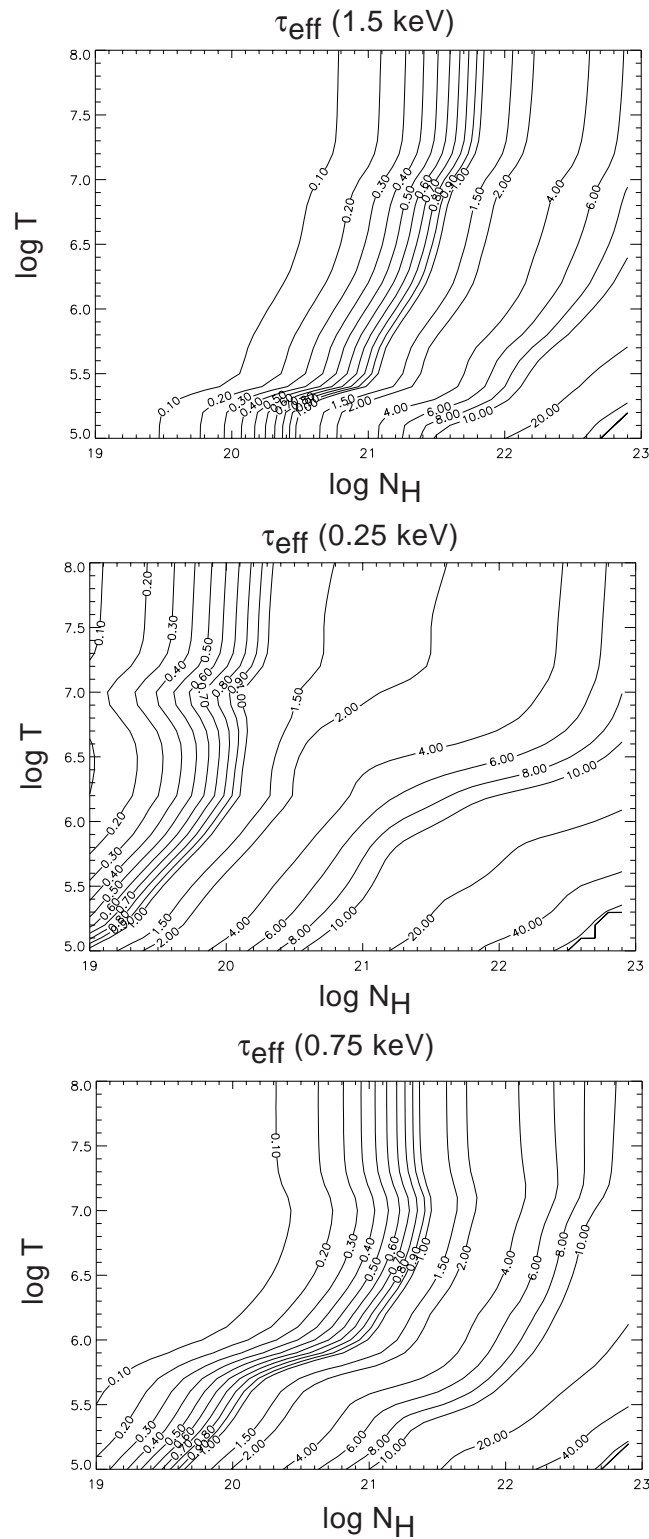


FIG. 13.—Contour plots of *ROSAT* band X-ray opacities as a function of temperature and column density for the 0.25, 0.75, and 1.5 keV bands

observed *ROSAT* count rates into X-ray intensities and luminosities. While this information somewhat duplicates Figure 9 of Snowden et al. (1997), we found the following format much more convenient.

*ROSAT* observations yield a detector energy-integrated intensity that we will denote by  $i_{\text{band}}^{\text{obs}}$  (counts s<sup>-1</sup> arcmin<sup>-2</sup>). The true detector intensity  $i_{\text{band}}$  of the object after correcting for foreground emission and intervening absorption is

$$i_{\text{band}}^{\text{corr}} = (i_{\text{band}}^{\text{obs}} - i_{\text{band}}^{\text{base}}) e^{\tau_{\text{band}}}(T, N). \tag{A1}$$

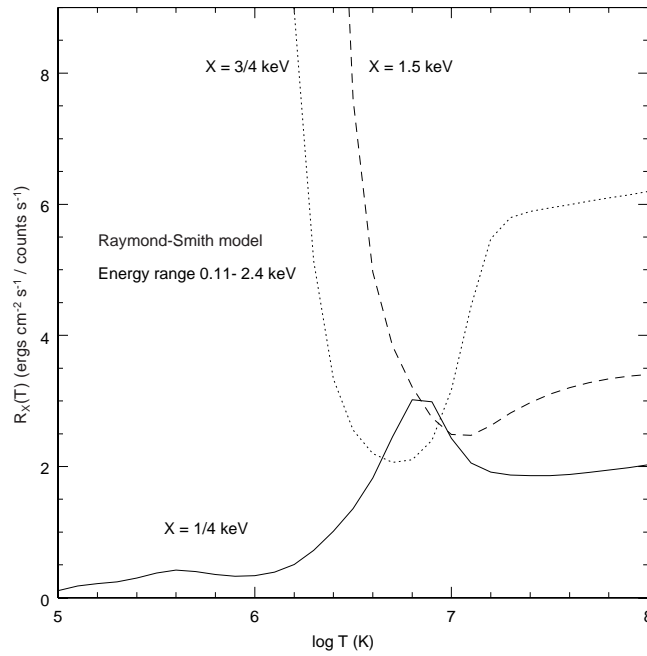


FIG. 14.—Conversion factor  $R(T)$  ( $\text{ergs cm}^{-2} \text{s}^{-1} / \text{counts s}^{-1}$ ) from detector counts to physical flux in the three *ROSAT* energy bands, over the energy range  $E = 0.11\text{--}2.4$  keV.

The intensity  $i_{\text{band}}^{\text{base}}$  is estimated by characterizing the emission in the area around the source of interest. It may arise because of local and totally unabsorbed foreground emission covering the entire section of sky of interest. It might also arise from partially absorbed emission from emitting gas between us and the target, where the emission is sufficiently uniform that its effect can be removed.

The absorption optical depth,  $\tau_{\text{band}}(T, N)$ , for each band is given in Figure 13 and requires a knowledge of (1) the total absorbing gas column  $N$  ( $\text{cm}^{-2}$ ), (2) the absorption cross section as a function of energy, and (3) the intrinsic spectrum of the emitting gas.

We discuss these ingredients in turn. (1) For the absorbing column, we have assumed that  $N = N(\text{H I})$ , which comes from the total H I column density measured in the direction of our source from either the NRAO or HB survey. This may overestimate the absorbing column by as much as a factor of a few, since we may be including in the column gas that lies beyond the source. However, we have also neglected the possibility of molecular hydrogen, which could be a large percentage of the neutral hydrogen, particularly at low latitudes. The effect of absorption associated with gas in ionized hydrogen regions should not be significant. The effects of these uncertainties on our final values are discussed in the main part of the text. (2) We have chosen to use the photoelectric absorption cross sections of Morrison & McCammon (1983). Although cross section data has been improved since this work (see Yan, Sadeghpour, & Dalgarno 1998, for example) and revisions in the elemental abundance set have been suggested (Mathis 1996; Savage & Sembach 1996), we continue to use this work for the sake of easy comparison and continuity. (3) Also for the sake of continuity, we use the standard thermal emission spectrum of Raymond & Smith (1977), noting that major improvements in X-ray emission calculations are currently underway (Liedahl, Osterheld, & Goldstein 1995).

Having obtained corrected detector intensities using equation (A1) and the opacity data in Figure 13, we convert this value to physical flux units. Multiplying the solid angle,  $\Omega$   $\text{arcmin}^{-2}$ , of the source by the mean detector intensity over this solid angle,  $\bar{i}_{\text{band}}$  gives the detector energy-integrated flux,

$$f_{\text{band}}(\text{counts s}^{-1}) = g \bar{i}_{\text{band}} \Omega . \quad (\text{A2})$$

The factor  $g$  is introduced as a shape factor, since conversion of intensity to flux requires some characterization of the geometry of the emitting region. Here we assume  $g = 1$ , but it can differ from this by to a factor of  $\sim 3$ .

Detector flux can be converted to true flux using

$$F_{E_{\text{min}}, E_{\text{max}}}(\text{ergs s}^{-1} \text{cm}^{-2}) = f_{\text{band}} R(T) , \quad (\text{A3})$$

where the conversion factor,  $R(T)$  ( $\text{ergs count}^{-1} \text{cm}^{-2}$ ), is given in Figure 14. This conversion factor depends upon the assumed input spectrum and the effective area of detector-telescope as a function of energy. It also depends upon the desired energy limits for the true flux. By assuming an intrinsic spectrum, it is possible to measure the flux over some small part of the spectrum and then infer the X-ray flux over a much wider energy range. It has become standard to quote X-ray fluxes and luminosities over the total energy range of *ROSAT*,  $E_{\text{min}} = 0.08$  keV to  $E_{\text{max}} = 2.4$  keV. In cases where there is a large absorbing column and concomitant large attenuation of the low-energy emission, however, the actual flux in the lower energy range becomes highly uncertain.

Finally, the total X-ray flux can be converted to X-ray luminosity assuming

$$L_{0.08,2.4 \text{ keV}} (\text{ergs s}^{-1}) = 4\pi d^2 F_{0.08,2.4 \text{ keV}}, \quad (\text{A4})$$

where  $d$  is the distance to the source.

#### REFERENCES

- Arnaud, K. A. 1996, in ASP Conf. Ser. 101, *Astronomical Data Analysis Software and Systems V*, ed. G. Jacoby & J. Barnes (San Francisco: ASP), 17
- Begelman, M. C., & Fabian, A. C. 1990, *MNRAS*, 224, 26P
- Benjamin, R. A., & Shapiro, P. R. 2000, *ApJS*, submitted
- Blitz, L., Fich, M., & Stark, A. A. 1982, *ApJS*, 49, 183
- Borkowski, K. J., Balbus, S. A., & Fristrom, C. C. 1990, *ApJ*, 355, 501
- Brinks, E., & Bajaja, E. 1986, *A&A*, 169, 14
- Brown, A. G. A., Hartman, D., & Burton, W. B. 1995, *A&A*, 300, 903
- Burrows, D. N., Singh, K. P., Nousek, J. A., Garmire, G. P., & Good, J. 1993, *ApJ*, 406, 97
- Cardelli, J. A., Clayton, G. C., & Mathis, J. S. 1989, *ApJ*, 345, 245
- Chu, Y.-H., Chang, H.-W., Su, Y.-L., & Mac Low, M. M. 1995, *ApJ*, 450, 157
- Chu, Y.-H., Mac Low, M. M., Guillermo, G.-S., Wakker, B., & Kennicutt, R. C. 1993, *ApJ*, 414, 213
- Clemens, D. R. 1985, *ApJ*, 295, 422
- Conti, P. S. 1975, in *H II Regions and Related Topics*, ed. T. L. Wilson & D. Downes (Heidelberg: Springer), 207
- Dame, T. M., Elmegreen, B. G., Cohen, R. S., & Thaddeus, P. 1986, *ApJ*, 305, 892
- Deul, E. R., & den Hartong, R. H. 1990, *A&A*, 229, 362
- Diplas, A., & Savage, B. D. 1994, *ApJ*, 424, 274
- Draine, B. T., & Anderson, N. 1985, *ApJ*, 292, 494
- Ferrier, K. 1998, *ApJ*, 503, 700
- Garmany, C. D., Conti, P. S., & Chiosi, C. 1982, *ApJ*, 263, 777
- Green, D. A. 1998, *A Catalogue of Galactic Supernova Remnants*, v. 1998 September (Cambridge: Mullard Rad. Astron. Obs.)<sup>5</sup>
- Haffner, L. M. 1999, Ph.D. thesis, Univ. Wisconsin-Madison
- Haffner, L. M., Reynolds, R. J., & Tuft, S. L. 1998, *ApJ*, 501, L83
- Hartmann, D., & Burton, W. B. 1997, *Atlas of Galactic Neutral Hydrogen* (New York: Cambridge Univ. Press) (HB)
- Heiles, C. 1979, *ApJ*, 229, 533
- . 1984, *ApJS*, 55, 585
- . 1990, *ApJ*, 354, 483
- Heiles, C., Reach, W. T., & Koo, B. C. 1988, *ApJ*, 332, 313
- Humphreys, R. M. 1978, *ApJS*, 38, 309
- Kamphuis, J., Sancisi, R., & van der Hulst, T. 1991, *A&A*, 244, L29
- Koo, B. C., Heiles, C., & Reach, W. T. 1992, *ApJ*, 390, 108
- Liedahl, D. A., Osterheld, A. L., & Goldstein, W. H. 1995, *ApJ*, 438, L115
- Lockman, F. J. 1989, *ApJS*, 71, 469
- Maciejewski, W., Murphy, E. M., Lockman, F. J., & Savage, B. D. 1996, *ApJ*, 469, 238
- Massa, D., Van Steenberg, M. E., Oliverson, N., & Lawton, P. 1998, in *Ultraviolet Astrophysics beyond the IUE Final Archive*, ed. W. Wamsteker & R. Gonzalez Riestra (ESA SP-413; Noordwijk: ESA), 723
- Mathis, J. S. 1996, *ApJ*, 472, 643
- Morrison, R., & McCammon, D. 1983, *ApJ*, 270, 119
- Penny, L. R. 1996, *ApJ*, 463, 737
- Pottasch, S. R., Wesselius, P. R., & Arnal, E. M. 1980, in *Second European IUE Conference*, ed. B. Battrock & J. Mort (ESA SP-157; Noordwijk: ESA), 13
- Raymond, J. C., & Smith, B. W. 1977, *ApJS*, 35, 419
- Reach, W. T., Wall, W. F., & Odegard, N. 1998, *ApJ*, 507, 507
- Reynolds, R. J. 1985, *ApJ*, 294, 256
- Reynolds, R. J., & Ogden, P. M. 1979, *ApJ*, 229, 942
- Savage, B. D., & Massa, D. 1987, *ApJ*, 314, 380
- Savage, B. D., & Sembach, K. R. 1996, *ARA&A*, 34, 279
- Savage, B. D., Sembach, K. R., & Lu, L. 1997, *AJ*, 113, 2158
- Sembach, K., & Savage, B. D. 1992, *ApJS*, 83, 147
- Sembach, K. R., Danks, A. C., & Savage, B. D. 1993, *A&AS*, 100, 107
- Sembach, K. R., Savage, B. D., & Tripp, T. M. 1997, *ApJ*, 480, 216
- Slavin, J. D., & Cox, D. P. 1992, *ApJ*, 392, 131
- Slavin, J. D., Shull, J. M., & Begelman, M. C. 1993, *ApJ*, 407, 83
- Snowden, S. L., Egger, R., Finkbeiner, D. P., Freyberg, M. J., & Plucinsky, P. P. 1998, *ApJ*, 493, 715
- Snowden, S. L., et al. 1995, *ApJ*, 454, 643
- . 1997, *ApJ*, 485, 125
- Tenorio-Tagle, G., & Bodenheimer, P. 1988, *ARA&A*, 26, 145
- Tomisaka, K., & Ikeuchi, S. 1986, *PASJ*, 38, 697
- Tuft, S. L. 1997, Ph.D. thesis, Univ. Wisconsin-Madison
- Wheelock, S. L., et al. 1991, *IRAS Sky Survey Atlas Explanatory Supplement* (Pasadena: IPAC-NASA)
- Yan, M., Sadeghpour, H. R., & Dalgarno, A. 1998, *ApJ*, 496, 1044

<sup>5</sup> Available on the World Wide Web at <http://www.mrao.cam.ac.uk/surveys/snrs/>.